

Kinetic model of the inner magnetosphere with arbitrary magnetic field

Raluca Ilie,¹ Michael W. Liemohn,² Gabor Toth,² and Ruth M. Skoug¹

Received 21 September 2011; revised 17 January 2012; accepted 25 February 2012; published 11 April 2012.

[1] Theoretical and numerical modifications to an inner magnetosphere model—Hot Electron Ion Drift Integrator (HEIDI)—were implemented, in order to accommodate for a nondipolar arbitrary magnetic field. While the dipolar solution for the geomagnetic field during quiet times represents a reasonable assumption in the near-Earth closed field region, during storm activity this assumption becomes invalid. HEIDI solves the time-dependent, gyration- and bounce-averaged kinetic equation for the phase space density of one or more ring current species. New equations are derived for the bounce-averaged coefficients for the distribution function, and their numerical implementation is discussed. Also, numerically solving all the bounce-averaged coefficients for the dipole case does not change the results significantly from the analytical approximation of Ejiri (1978). However, distorting the magnetic field changes all bounce-averaged coefficients that make up the kinetic equation. Initial simulations show that changing the magnetic field changes the whole topology of the ring current. This is because the drifts are altered due to dayside compression and nightside stretching of the field. Therefore, at certain locations, the nondipolar magnetic drifts can dominate the convective drifts, considerably altering the pressure distribution in the equatorial plane.

Citation: Ilie, R., M. W. Liemohn, G. Toth, and R. M. Skoug (2012), Kinetic model of the inner magnetosphere with arbitrary magnetic field, *J. Geophys. Res.*, 117, A04208, doi:10.1029/2011JA017189.

1. Introduction

[2] Numerous studies, both data analysis and numerical simulations, have attempted to unravel the complex processes that control the nature, transport, and losses of the ring current population. Statistical studies involving large databases of in situ magnetic field measurements in the inner magnetosphere [Lui, 2003; Tsyganenko *et al.*, 2003; Jorgensen *et al.*, 2004; Le *et al.*, 2004] showed that under disturbed conditions, large depressions in the geomagnetic field strength (down to ~ -400 nT) are associated with the ring current.

[3] The configuration of the storm time ring current changes dramatically depending on the storm phase and has a strong dependence on the magnetic local time (MLT) [e.g., Brandt *et al.*, 2002]. The ring current induced magnetic field alters the grad B and curvature drift velocities of all the trapped particles [e.g., Ebihara and Ejiri, 2000]. Several empirical models of the ring current-induced magnetic field [e.g., Kim and Chan, 1997; Nakamura *et al.*, 1998] attempted to quantify the adiabatic changes of the ring current population using empirical magnetic field models that are a function of the geocentric distance and Dst.

[4] The coupling between plasma and fields in the inner magnetosphere plays a key role in the overall behavior of the magnetosphere. In the inner magnetosphere, plasma does not behave like a fluid, therefore a kinetic description of this region is needed. While most kinetic models treat the plasma transport realistically, they lack a consistent treatment of the fields, that is, a dipolar assumption is used in the description of the magnetic field along with empirical formalisms for the electric fields [Fok *et al.*, 1993; Chen *et al.*, 1993; Liemohn *et al.*, 1999]. On the other hand, MHD numerical models have self consistency but they lack the ability to reproduce essential gradient curvature drifts and their description of the inner magnetosphere is overly simplified.

[5] A realistic time-varying magnetic field is crucial for understanding the ring current and plasma sheet dynamics, especially during magnetic activity. Several ring current simulations that incorporate a self-consistent magnetic field have been developed. One example is the Rice Convection Model (RCM) coupled with the magnetofriction (MF) code of Toffoletto *et al.* [2003], an inner magnetospheric model which self-consistently accounts for the inner magnetospheric currents in calculating the magnetospheric B field configuration and also accounts for the coupling between these currents with ionospheric currents. Using this configuration, Lemon *et al.* [2004] obtained a force-balanced magnetic field by solving a set of ideal magnetohydrodynamic (MHD) equations with a frictional dissipation term. Their simulation results of the plasma transport from the plasma sheet to the ring current suggest that the perturbation associated with the injection of plasma sheet ions in the

¹Space Science and Applications, Los Alamos National Laboratory, Los Alamos, New Mexico, USA.

²Department of Atmospheric, Oceanic, and Space Sciences, University of Michigan, Ann Arbor, Michigan, USA.

inner magnetosphere inhibits the formation of a significant ring current. Several models have been developed that use the T96 or T01 magnetic field model [Tsyganenko, 1995; Tsyganenko and Stern, 1996; Tsyganenko, 2002], that take IMF and Dst as inputs [Fok and Moore, 1997; Fok et al., 2001; Ganushkina et al., 2001; Ganushkina and Pulkkinen, 2002; Vapirev and Jordanova, 2007]. Zaharia et al. [2006] solved quasi 2-D elliptic equations to obtain a self-consistent magnetic field expressed by the Euler potentials. Comparison with a dipolar configuration shows that depressions of the plasma pressure on the nightside are lower (higher equatorial perpendicular pressure) when the magnetic field is consistently accounted for. Two way coupling between a ring current model [Jordanova et al., 2006] and this 3-D plasma force balance model [Zaharia et al., 2008] also shows significant differences in the inner magnetosphere compared to the case when the ring current model is based on a dipolar approximation.

[6] Another study by Chen et al. [2006] used a tracing method for the equatorially mirroring ions under a self-consistent magnetic field, extrapolating the particle pressure along the field line with an assumed equatorial pitch angle distribution, and showed that the self-consistent feedback between the plasma pressure and the magnetic field suppresses ring current energization. Liu et al. [2006] reported on the need of a consistent representation of the fields in an inner magnetosphere model and showed that their magnetically self-consistent model reasonably reproduced many of the general features of the storm time ring current.

[7] Moreover, Liemohn and Brandt [2005] discussed electric field feedback as a limiter of future ring current enhancement. Numerical simulations of the ring current and plasmasphere indicate that an accurate description of the electric field is essential in reproducing their large-scale morphology and bulk parameters [Liemohn et al., 2004, 2006]. Ridley and Liemohn [2002] and Ebihara et al. [2005] also commented on this nonlinear feedback, suggesting that strong electric fields in the inner magnetosphere as observed by CRRES [Wygant et al., 1998; Rowland and Wygant, 1998] are of ring current origin.

[8] On the other hand, De Zeeuw et al. [2004] presented initial results of self consistent RCM coupling with the BATS-R-US MHD model. The authors report on the inflation of the magnetic field in the tail due to the presence of the ring current. With a similar setup, Zhang et al. [2007] performed a real storm simulation using the coupled RCM-MHD code now as part of the Space Weather Modeling Framework (SWMF) [Tóth et al., 2005, 2012]. Their simulation results are in good agreement with geosynchronous plasma and fields observations. Other studies using RCM in conjunction with a realistic magnetic field from MHD model have shown that the global magnetosphere responds nonlinearly to solar wind energy inputs [Ilie et al., 2010b] and that a certain signal-to-noise ratio is needed for a periodicity to penetrate to the inner magnetosphere [Ilie et al., 2010a].

[9] Nevertheless, the RCM model has the disadvantage that it assumes an isotropic pitch angle distribution and charge exchange processes are not explicitly considered (at least not in the version of RCM used in the SWMF).

[10] The Hot Electron Ion Drift Integrator model was extensively used in previous years and just a few relevant findings are detailed below. A numerical study by Liemohn

et al. [1999] suggests that dayside ion flow-out is the major ring current loss process during the main phase of intense magnetic storms and the eastward component of the solar wind electric field sets up the timescale for ion loss due to these drifts. Elevated convection corroborated with decreasing plasma sheet density will lead to a gradual replacement of the higher-density plasma with the lower density plasma on the open drift trajectories, yielding a significant loss of ring current energy. Conversely, if the plasma sheet density remains high but the convection strength gradually decreases, then newly injected high-density plasma will move along open drift paths at higher radial distances. Liemohn and Kozyra [2005] show that the former scenario leads to a two phase decay of the ring current, while the latter is producing a single dip storm profile. Kozyra and Liemohn [2003] show that the ion flow-out losses dominate the main phase of the storm while the charge exchange processes are significantly contributing to the ring current decay during the recovery phase. The convection strength controls this loss process, that is, increasing convection will increase the flow-out loss and vice versa.

[11] Due to the long duration of a magnetic storm, the particles that are injected on the nightside are able to drift completely through the inner magnetosphere. This drift is energy- and convection-dependent and therefore, under times of high convection, it can take only a few hours for the energetic particles moving on open drift paths to reach the magnetopause and to be lost. Liemohn et al. [2001] and Kozyra et al. [2002] suggest that during this time the ring current is highly asymmetric, and most of its energy (up to 90%) is flowing along open drift paths.

[12] Another important finding comes from Liemohn et al. [2005] who seek to quantify the influence of nightside conductance morphology and intensity on the storm time ring current and plasmasphere. Their work reveals the existence of an optimal conductance level for maximal ring current intensity. That is, it is shown that too little conductance leads to large shielding potentials that effectively inhibit ring current growth. On another hand too much conductance leads to continual flow-through of the hot ions therefore no build up of the ring current.

[13] In this paper we describe the changes to the Hot Electron Ion Drift Integrator (HEIDI) model, that includes both charge exchange losses as well as full pitch angle distributions and therefore, pitch angle-dependent drifts and losses, so it can handle arbitrary magnetic fields. A similar alternative to modifying HEIDI would be to use the nondipolar version of RAM [e.g., Jordanova et al., 2006; Vapirev and Jordanova, 2007], which also solves the pitch angle-dependent hot ion drift motion on an equatorial plane grid. Presented below is the complete set of equations for implementing a nondipolar magnetic field in a drift physics model with an equatorial plane spatial grid.

2. The Model

[14] The Hot Electron Ion Drift Integrator model is the Liemohn et al. [2004] version of the Ring Current Atmosphere Interaction Model (RAM) based on earlier versions by Fok et al. [1993] and Jordanova et al. [1996], developed at the University of Michigan. It computes the time-dependent, gyration- and bounce-averaged kinetic equation

for the phase space density of one or more ring current species (e , H^+ , He^+ , O^+) on an equatorial based grid. The bounce-averaged kinetic equation,

$$\begin{aligned} \frac{\partial Q}{\partial t} + \frac{1}{R_0^2} \frac{\partial}{\partial R_0} \left(R_0^2 \left\langle \frac{dR_0}{dt} \right\rangle Q \right) + \frac{\partial}{\partial \phi} \left(\left\langle \frac{d\phi}{dt} \right\rangle Q \right) \\ + \frac{1}{\sqrt{E}} \frac{\partial}{\partial E} \left(\sqrt{E} \left\langle \frac{dE}{dt} \right\rangle Q \right) + \frac{1}{h(\mu_0)\mu_0} \frac{\partial}{\partial \mu_0} \\ \cdot \left(h(\mu_0)\mu_0 \left\langle \frac{d\mu_0}{dt} \right\rangle Q \right) = \left\langle \frac{\delta Q}{\delta t} \right\rangle_{collisions} \end{aligned} \quad (1)$$

solves for the phase space distribution function $Q(R_0, \phi, E, \mu_0, t)$, where R_0 represents the radial distance in the equatorial plane, ϕ is the geomagnetic east longitude ($\phi = 0$ at midnight), E is the kinetic energy of the particle and $\mu_0 = \cos \alpha_0$, where α_0 is the particle equatorial pitch angle.

[15] The various terms of equation (1) describe changes in the distribution function due to loss processes generated by flow of plasma out to the dayside outer boundary, collisionless drifts, energy loss and pitch angle scattering due to Coulomb collisions with the thermal plasma, charge exchange loss with the hydrogen corona, and precipitative loss to the upper atmosphere (included in the left hand side term). Time, geocentric distance in the equatorial plane, magnetic local time, kinetic energy, and cosine of the equatorial pitch angle are the five independent variables. The distribution function in both space and velocity space can be computed in HEIDI for all pitch angles and local times, with an energy range typically spanning 10 eV to 400 keV and L shell values ranging from 2 to 6.5.

[16] The brackets $\langle \rangle$ in equation (1) denote bounce-averaging and for a quantity χ and is defined as the following:

$$\langle \chi \rangle = \frac{1}{S_B} \int_{s_m}^{s_{m'}} \chi \frac{ds}{\sqrt{1 - \frac{B(s)}{B_m}}} \quad (2)$$

where $B(s)$ is the magnetic field along the field line, s is the distance from the ionospheric foot point along the field line, B_m represents the magnitude of the magnetic field at the mirror points s_m and $s_{m'}$ and finally S_B represents the half-bounce path length ($S_B = \int_{s_m}^{s_{m'}} \frac{ds}{\sqrt{1 - \frac{B(s)}{B_m}}} = 2R_0 h$), as defined by *Roederer*

[1970]. Moreover, the function h in equation (1) is related to the half-bounce period of the particles.

$$h = \frac{1}{2R_0} \int_{s_m}^{s_{m'}} \frac{ds}{\sqrt{1 - \frac{B(s)}{B_m}}} \quad (3)$$

An accurate description of the convection electric field is very important for a complete description of the ring current. HEIDI includes a variety of electric field models: empirical Volland-Stern two-cell convection pattern [*Volland, 1973; Stern, 1975; Maynard and Chen, 1975*], modified McIlwain E5D model [*McIlwain, 1986; Liemohn et al., 2001*] along with a self-consistent electric field described by *Liemohn et al. [2004]* and *Liemohn and Kozyra [2005]*. The Volland-Stern model for the electric field is based on the Kp index dependence with a shielding factor of $\gamma = 2$ as determined by *Maynard and Chen [1975]*. The McIlwain model uses boundary conditions derived from the Defense Meteorological Satellites Program (DMSP) along with a Weimer model generated transpolar

potential. The self consistent model for the electric field employs coupling with the Ridley Ionosphere Model (RIM), given that the field aligned currents calculated by HEIDI are used as source terms in the Poisson equation for the ionospheric potential, solved by RIM [*Ridley and Liemohn, 2002; Ridley et al., 2004*]. *Liemohn et al. [2006]* quantify the accuracy of these models in order to determine the electric field morphology that allows the best ring current representation.

[17] The source term for the phase space density equation is provided by the nightside outer boundary of the simulation domain. That is, geosynchronous observations of particle fluxes are used as input functions. The composition of the plasma sheet is assumed to have Kp dependence and is described using the empirical formulation of *Young et al. [1982]*. However, *Ganushkina et al. [2006]* show that ring current models are very sensitive to the choice of the initial and boundary conditions and these have significant effects on the modeled ring current intensity. For more details about the numerical model, see the work of *Liemohn et al. [1999, 2001, 2004]*.

2.1. Dipole Field Model

[18] Along with an accurate description of the electric field, the magnetic field plays a major role when modeling the ring current since the magnetic gradient curvature along with the $\vec{E} \times \vec{B}$ drift velocities determine the particle's total drift at ring current energies. In a dipolar magnetic field, the gradient curvature drift can be approximated by the analytical formulation of *Ejiri [1978]*:

$$\langle \vec{V}_{GC} \rangle = -\frac{3ER_0^2}{qM_e} \left(1 - \frac{I(\mu_0)}{6h(\mu_0)} \right) \hat{\phi} \quad (4)$$

where q is the charge of the particle and M_e is the dipole moment of the Earth. I is a quantity related with the second adiabatic invariant and is defined by:

$$I = \frac{1}{R_0} \int_{s_m}^{s_{m'}} ds \sqrt{1 - \frac{B(s)}{B_m}} \quad (5)$$

[19] Since any point along a field line can be used to track the $E \times B$ drift across flux tubes, we choose the equator as the reference plane so the bounce-averaged drift velocity is determined from the equatorial field [*Roederer, 1970*]:

$$\langle \vec{V}_D \rangle = \frac{\vec{E}_0 \times \vec{B}_0}{B_0^2} = \left\langle \frac{dR_0}{dt} \right\rangle + \left\langle \frac{d\phi}{dt} \right\rangle \quad (6)$$

where $E_0 = -\nabla(U_{convection} + U_{corotation})$ and $U_{corotation} = -\frac{C}{R_0}$ with $C = 0.0144 R_e^2 V m^{-1}$.

[20] In the absence of parallel electric fields and assuming the particles move in a dipolar magnetic field configuration, the bounce-averaged rate of change of the cosine of the equatorial pitch angle and the bounce-averaged rate of change of the particle's kinetic energy over a bounce period [*Ejiri, 1978*] are:

$$\left\langle \frac{d\mu_0}{dt} \right\rangle = \frac{1 - \mu_0^2}{4R_0\mu_0} \frac{I(\mu_0)}{h(\mu_0)} \left\langle \frac{dR_0}{dt} \right\rangle \quad (7)$$

$$\left\langle \frac{dE}{dt} \right\rangle = -\frac{3E}{R_0} \left(1 - \frac{I(\mu_0)}{6h(\mu_0)} \right) \left\langle \frac{dR_0}{dt} \right\rangle \quad (8)$$

[21] The $h(\mu_0)$ and $I(\mu_0)$ integrals, as defined by equations (3) and (5), are evaluated using the approximations of *Ejiri* [1978], valid only for a dipole magnetic field. Therefore, the $\langle \frac{d\mu_0}{dt} \rangle$ and $\langle \frac{dE}{dt} \rangle$ quantities are dependent solely on the radial distance in the equatorial plane and pitch angle, as the $h(\mu_0)$ and $I(\mu_0)$ are only pitch angle-dependent.

2.2. Arbitrary Magnetic Field Model

[22] Extensive modifications of the HEIDI model were carried out in order to accommodate for a nondipolar magnetic field. This involves the development of new theoretical formulations for the bounce-averaged coefficients, to replace the previously used analytical approximations of *Ejiri* [1978]. The new model is valid for arbitrary magnetic fields including any empirical or analytical descriptions. Moreover, this generalized formalism is eliminating the assumption that the equatorial plane is the plane of minimum magnetic field. Therefore it contains a generalized description of the particles drift. Details of the derivations are described in Appendix A.

[23] The bounce-averaged rate of change of the cosine of the particle's pitch angle is derived assuming the conservation of the magnetic moment μ_m and the second adiabatic invariant J and for an arbitrary magnetic field can be written as:

$$\begin{aligned} \left\langle \frac{d\mu_0}{dt} \right\rangle = & -\frac{(1-\mu_0^2)I}{2h\mu_0} \left\{ v_{0R} \left(\frac{1}{2B_0} (\nabla B_0)_{\hat{R}_0} + \frac{1}{R_0} + \frac{1}{I} (\nabla I)_{\hat{R}_0} \right) \right. \\ & \left. + v_{0\phi} \left(\frac{1}{2B_0} (\nabla B_0)_{\hat{\phi}} + \frac{1}{I} (\nabla I)_{\hat{\phi}} \right) + \frac{1}{2B_0} \frac{\partial B_0}{\partial t} + \frac{1}{I} \frac{\partial I}{\partial t} \right\} \end{aligned} \quad (9)$$

where B_0 represents the equatorial value of the magnetic field. As opposed to the dipole field case (see equation (7)), $\langle \frac{d\mu_0}{dt} \rangle$ has a more complex description, depending explicitly on the magnetic field gradients, equatorial drifts and pitch angle. Moreover, the I and h quantities are now varying with the equatorial radial distance, pitch angle, and for time varying magnetic fields, time.

[24] Additionally, the bounce-averaged rate of change of the kinetic energy of the particle is derived from the conservation of the first adiabatic invariant and for the case of no parallel electric fields, the general form is:

$$\begin{aligned} \left\langle \frac{dE}{dt} \right\rangle = & \frac{E}{B_0} \left(1 - \frac{I}{2h} \right) \frac{\partial B_0}{\partial t} + E v_{0R} \left(\frac{1}{B_0} \left(1 - \frac{I}{2h} \right) (\nabla B_0)_{\hat{R}_0} \right. \\ & \left. - \frac{1}{h} \left(\frac{I}{R_0} + (\nabla I)_{\hat{R}_0} \right) \right) + E v_{0\phi} \left(\frac{1}{B_0} \left(1 - \frac{I}{2h} \right) (\nabla B_0)_{\hat{\phi}} \right. \\ & \left. - \frac{1}{h} (\nabla I)_{\hat{\phi}} \right) - \frac{E}{h} \frac{\partial I}{\partial t} \end{aligned} \quad (10)$$

[25] The description of $\langle \frac{dE}{dt} \rangle$ is also more involved than the one for the case of a dipole field (see equation (8)), containing dependencies on the magnetic field gradients, pitch angles as well as temporal variations of B_0 . However, substituting a dipolar magnetic field in equations (9) and (10) we obtain the *Ejiri* [1978] formulae (equations (7) and (8), respectively).

[26] The analytical approximation of *Ejiri* [1978] for the bounce-averaged gradient-curvature drift (equation (4)) is

replaced by the bounce average of the following general formula, that now includes both contributions from the azimuthal and radial components,

$$\vec{V}_{GC} = -\frac{m_i}{qB^4} \left(v_{\parallel}^2 + \frac{v_{\perp}^2}{2} \right) \left[\left(\nabla \frac{B^2}{2} \right) \times \vec{B} \right] \quad (11)$$

where m_i is the ion mass and v_{\parallel} and v_{\perp} represent its parallel and perpendicular velocity. Moreover, all bounce-averaged quantities that make up the terms in equation (1) (e.g., geocorona hydrogen density $\langle H_{density} \rangle = \frac{1}{S_B} \int_{m_1}^{m_2} n_H \frac{ds}{1-\frac{B(s)}{B_m}}$) are numerically calculated, for an arbitrary magnetic field. The model described above is valid for arbitrary magnetic fields, including empirical magnetic field models. The details of the numerical implementation and testing are described in sections 3, 4, and 5.

3. Implementation of Numerical Integrals of I and h

[27] The first step to arbitrary magnetic field representation in HEIDI was to replace the analytical formulae for I (equation (5)) and h (equation (3)) with numerical integrals along the field line. To do so, the integration was performed assuming that the magnetic field varies linearly in between two consecutive grid points along the field line and the value of the integral was analytically estimated between any two neighboring grid points. That is:

$$I = \frac{1}{R_0} \sum_i \frac{2}{3} \frac{1}{\sqrt{B_m}} \frac{s_{i+1} - s_i}{B_i - B_{i+1}} \left((B_m - B_{i+1})^{3/2} - (B_m - B_i)^{3/2} \right) \quad (12)$$

$$h = \frac{1}{2R_0} \sum_i 2\sqrt{B_m} \frac{s_{i+1} - s_i}{B_i - B_{i+1}} \left((B_m - B_{i+1})^{1/2} - (B_m - B_i)^{1/2} \right) \quad (13)$$

where ds_i is the length of the field line element at the current grid point. At the mirror points I and h become

$$\Delta I_m = \frac{2}{3} \frac{1}{\sqrt{B_m}} \Delta s \sqrt{(B_m - B_i)} \quad (14)$$

$$\Delta h_m = 2\sqrt{B_m} \frac{\Delta s}{\sqrt{B_m - B_i}} \quad (15)$$

where

$$\Delta s = \frac{(B_m - B_i)(s_i - s_{i-1})}{B_{i-1} - B_i} \quad (16)$$

is the estimated length of the last field line segments within the mirror points.

[28] This approximation avoids the singularities occurring at the mirror points in the calculation of h . Moreover, this method gives much more accurate results than using a simple trapezoidal integration rule. The grid along the field line is uniform in latitude and symmetric with respect to the equatorial plane. Nevertheless, this means that the grid is not uniform in the element of the field line length, although HEIDI can accommodate nonuniform grids as well (e.g.,

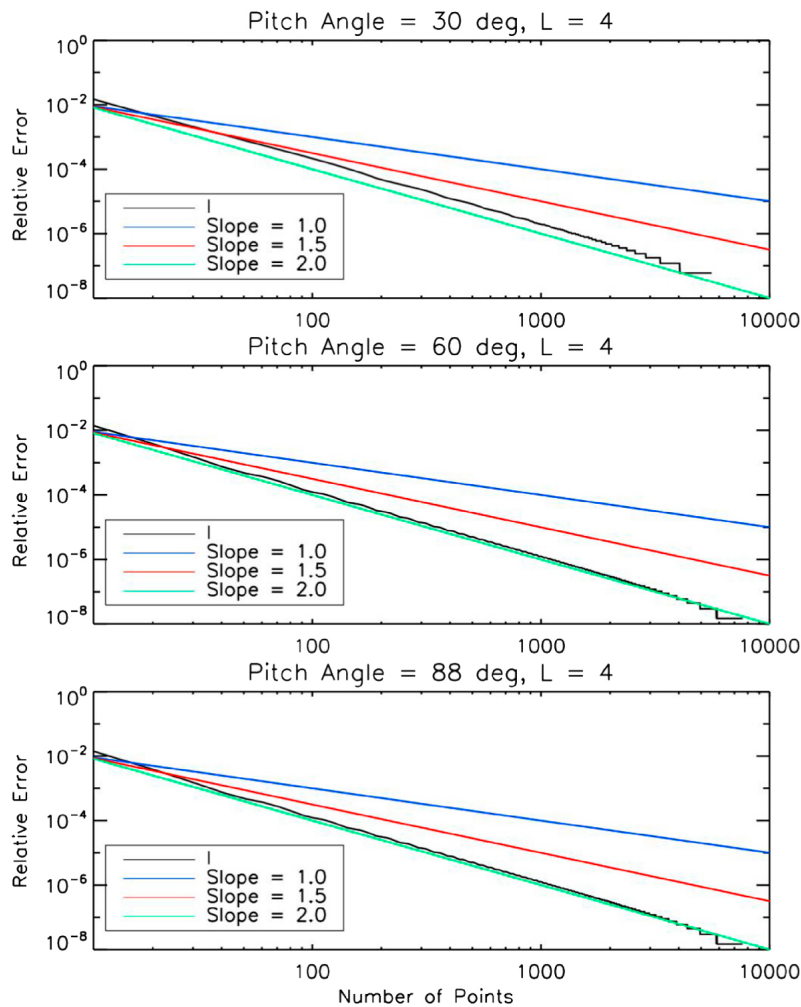


Figure 1. Relative error for I calculations versus number of points along a field line for three choices of pitch angle: (top) 30° , (middle) 60° , and (bottom) 88° for L shell = 4. Black line shows the results of the integral, while the blue, red, and green lines show slopes of 1, 1.5, and 2, respectively.

field aligned grids that are more refined in the equatorial region, to better resolve the equatorially mirroring particles).

[29] Figure 1 presents the numerical integration results of $I = \frac{1}{R_0} \int_{s_m}^{s_m'} ds \sqrt{1 - \frac{B(s)}{B_m}}$ for three choices of the particle's pitch angle: 30° (Figure 1, top), 60° (Figure 1, middle), and 88° (Figure 1, bottom) for a L shell value of 4. The choice of 88° pitch angle was made in order to illustrate the profile of these parameters for nearly equatorially mirroring particles. For easy reference, in each plot the blue, red and green lines have constant slopes of 1.0, 1.5 and 2.0, respectively. This is a proxy for the order of accuracy of the integration method. Note that the scale is logarithmic. The relative error was calculated as the difference between the true value (the value of the integral for a very refined grid, in our case 100001 points) and the value of the I integral for $nPoint$ grid size. We use the trapezoidal-like rule to evaluate the integral, which results in second-order accuracy.

[30] Similarly to Figure 1, Figure 2 shows the integration results for $h = \frac{1}{2R_0} \int_{s_m}^{s_m'} \frac{ds}{\sqrt{1 - \frac{B(s)}{B_m}}}$. Since this expression contains

a singularity at the mirror points, our method of linearizing the magnetic field in between two consecutive field line grid points is less accurate than second order. The 1.5 convergence rate and the fluctuations seen in the behavior of h are due to the fact that the integration on the last segment has a relatively large contribution to the total value of the integral. However, this is a good method for the purpose of our work and both integrals are converging quite fast for a reasonably sized field aligned grid, that is 101 points.

[31] To further reinforce our choice of 101 grid points, Figure 3 (left) shows the relative error to the converged value (black line) and the relative error to the analytical value (the value as provided by *Ejiri* [1978] formula) for the three choices of pitch angle described above. On the right, we show a close-up of the same plots on the left. A dotted blue line marks the 101 point choice. Only the X axis is logarithmic for this plot. We note that the relative error for both comparisons is under 0.1%. However, the *Ejiri* [1978] expressions for I and h are numerical approximations as well and not analytical solutions (although for simplicity we

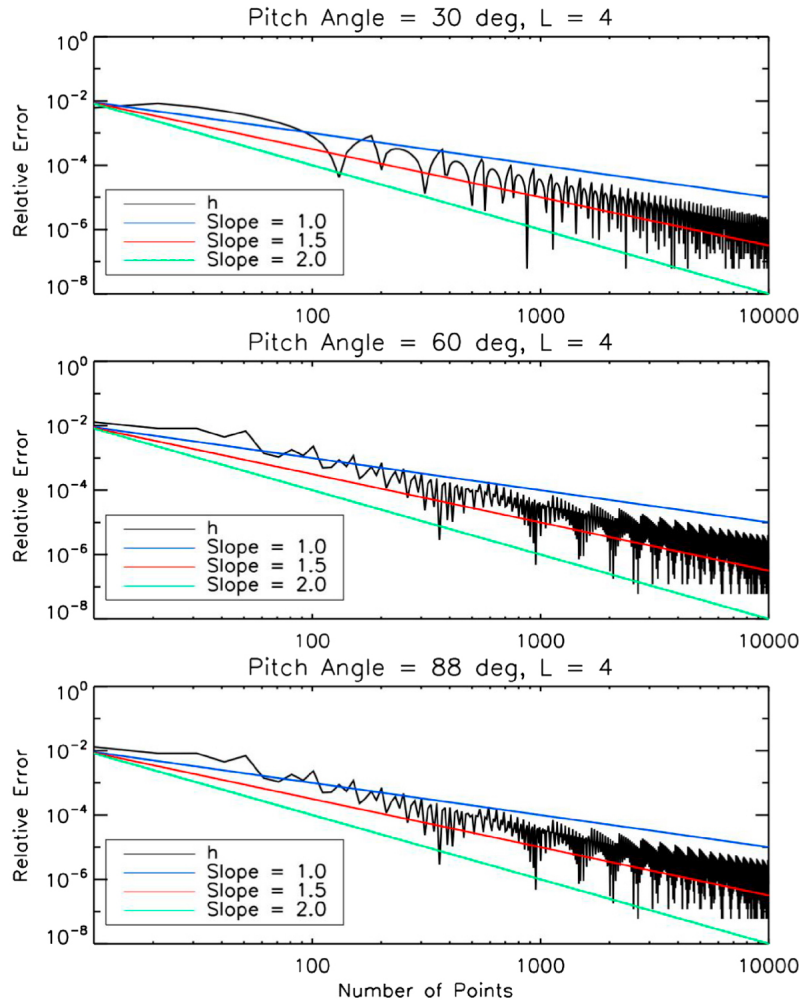


Figure 2. Relative error for h calculations versus number of points along a field line for three choices of pitch angle: (top) 30° , (middle) 60° , and (bottom) 88° for L shell = 4. Black line shows the results of the integral, while the blue, red, and green lines show slopes of 1, 1.5, and 2, respectively.

refer to them as “analytical,” because they are expressed as a trigonometric polynomial function).

[32] Figure 4 is a replica of Figure 3, only now for the h integration results. Again, the relative difference between both the converged and analytical values are under 1% for all pitch angles for 101 grid points along the magnetic field line.

4. Nondipolar Field Specifications

[33] To illustrate the differences between the dipolar and nondipolar HEIDI, extensive tests were performed using an idealized magnetic field configuration, that is a stretched dipole with a stretching factor that is local time-dependent. The dipolar magnetic field is stretched in the X direction by a factor $\alpha = a + b \cdot \cos \phi$, where a and b are two constants which determine the extent of the stretching. If α is constant for constant ϕ , then its gradient is orthogonal to the radial vector and the resulting field is divergence free. Therefore, α can only depend on the azimuthal angle, otherwise the divergence free condition for the magnetic field would not

be met. The resulting field and its components expressed in cartesian coordinates are:

$$B_x = \frac{1}{\alpha} \frac{3z\alpha}{\left((x\alpha)^2 + y^2 + z^2\right)^{\frac{3}{2}}} \hat{e}_x \quad (17)$$

$$B_y = \frac{3zy}{\left((x\alpha)^2 + y^2 + z^2\right)^{\frac{3}{2}}} \hat{e}_y \quad (18)$$

$$B_z = \frac{2z^2 - x^2\alpha^2 - y^2}{\left((x\alpha)^2 + y^2 + z^2\right)^{\frac{3}{2}}} \hat{e}_z \quad (19)$$

Note that the $\frac{1}{\alpha}$ stretching factor only appears in the B_x formula so only B_x is being compressed or stretched. However, α appears in all 3 formulas, therefore all components are modified by it.

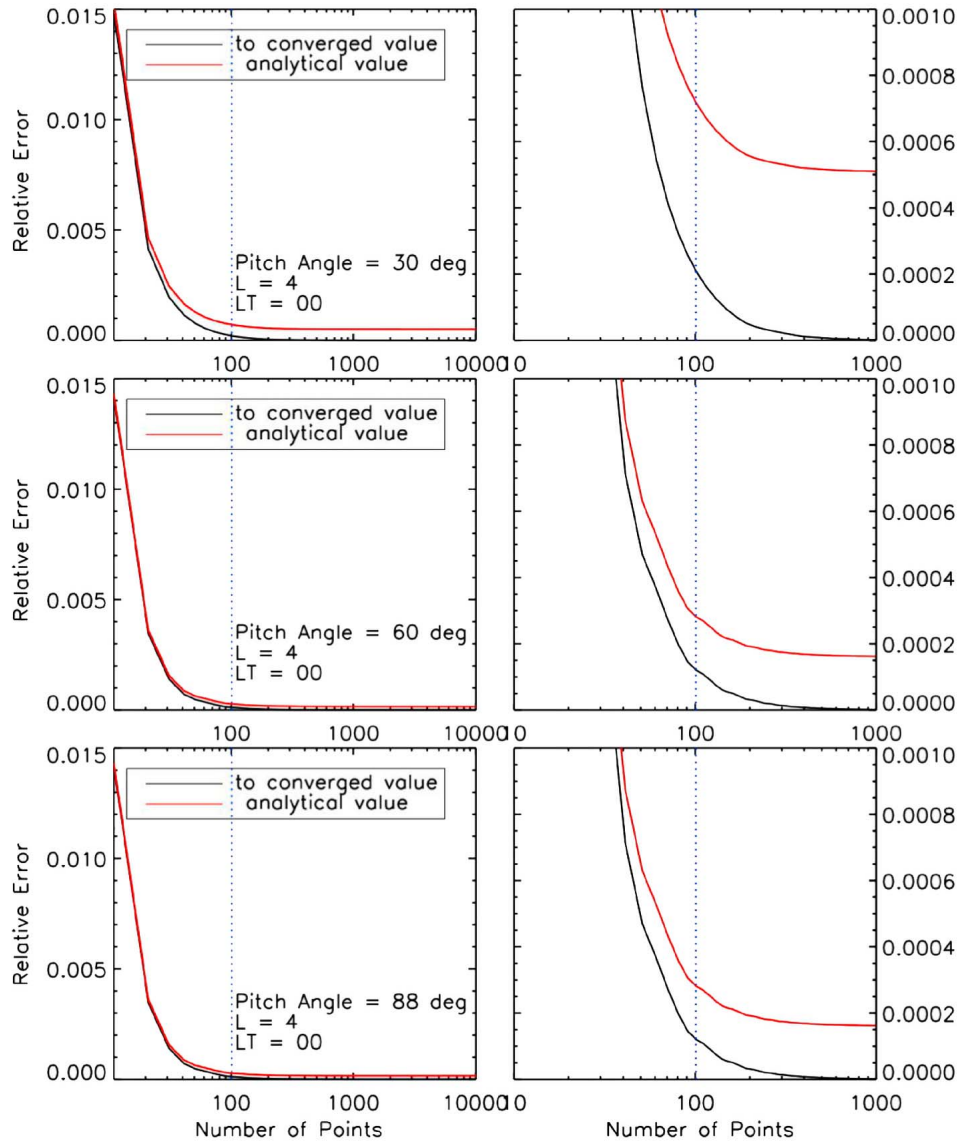


Figure 3. Relative error of the results of numerical integration of I for three choices of pitch angle: (top) 30° , (middle) 60° , and (bottom) 88° for L shell = 4 and local time (LT) = 0.0. Close-ups of the profile are shown on the right. Note that the x axis is logarithmic.

[34] The motivation behind this choice is that this configuration provides us with a simple, intuitive, nondipolar solution for the magnetic field that can be easily tested. When the stretching is approaching zero, namely the magnetic field would approach the dipolar configuration, we are able to recover the dipole solution. The HEIDI model run including only two ring current species (H^+ and O^+), with a Volland-Stern electric field [Volland, 1973; Stern, 1975]. The field aligned grid size was set to 101 points. Furthermore, this testing also enabled us with a measure of how much the distribution function changes when not only the magnetic field is not dipolar but also the bounce-averaged coefficients are calculated consistently.

[35] To get a better picture of the magnetic field stretching, Figure 5 shows the ratios between the magnetic field magnitude of a dipole and the magnitude of the stretched dipole

with $a = 1.0$ and $b = 0.1$ (Figure 5, left) and with $a = 1.0$ and $b = 0.2$ (Figure 5, right) in the equatorial plane. Comparing the values of the magnetic field magnitude for the stretched versus nonstretched configuration, we see that the stretching coefficient $b = 0.1$ is equivalent to a reduction of the field on the nightside to $2/3$ of the dipole value while the dayside is compressed by roughly the same amount. However, on the dusk and dawn sides the field has dipolar values ($B_{dipole}/B_{stretched} = 1.0$). Similarly, for $b = 0.2$ the distortion is double that for the dipole case, with the values of $B_{stretched}$ on the dayside significantly higher for the nondipolar cases, while the nightside magnetic field displays increased depression with increasing stretching (larger b). Another advantage of using this magnetic field for testing is that it resembles the Earth's magnetic field during disturbed conditions.

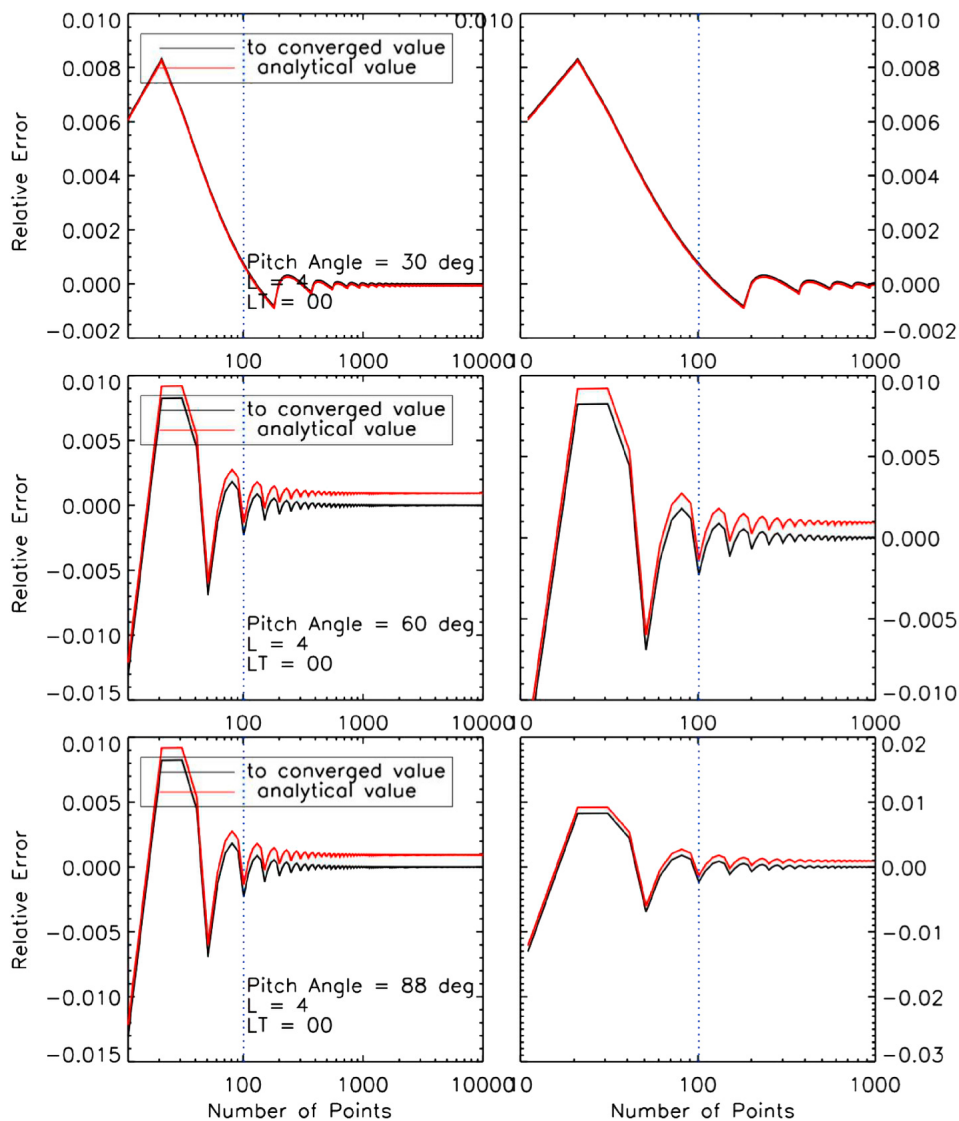


Figure 4. Relative error of the results of numerical integration of h for three choices of pitch angle: (top) 30° , (middle) 60° , and (bottom) 88° for L shell = 4 and local time (LT) = 0.0. Close-ups of the profile are shown on the right. Note that the x axis is logarithmic.

[36] For easy reference, the field lines in the $y = 0$ plane are shown in Figure 6. Red lines show the dipolar magnetic field lines, while the blue, green, and orange lines show the field lines for an asymmetrically stretched dipole with distortion factors of $b = 0.1$, $b = 0.2$, and $b = 0.4$, respectively. The stretched field lines start on the same latitude grid (have the same foot points) as the dipole field, so the differences represent the stretching.

[37] Figure 7 presents dial plots of the I results for 30° (Figures 7a–7c), 60° (Figures 7d–7f), and 88° (Figures 7g–7i) equatorial pitch angles for a dipolar magnetic field (Figures 7a, 7d, and 7g), an asymmetrically stretched dipole field with distortion factor $b = 0.1$ (Figures 7b, 7e, and 7h), and an asymmetrically stretched dipole field with distortion factor $b = 0.2$ (Figures 7c, 7f, and 7i). For the case of the dipole, the values of I are relatively constant, in agreement with the analytical formula of *Ejiri* [1978], which shows only dependence

on the pitch angle and predicts a constant value, independent of the radial distance. Nevertheless, for nearly equatorially mirroring particles ($\alpha_0 = 88^\circ$) in a dipole magnetic field, the values of I display small radial gradients with azimuthal symmetry and span over a larger range. This is due to numerical artifacts of the integration since the integration domain is small for large pitch angles and therefore the numerical errors are largest for our uniform grid. Also, the density of points along the field line decreases with increasing radial distance and therefore the solution is less accurate the farther away we go from the inner boundary. However, as the particle's equatorial pitch angle decreases, the numerical integration provides a more uniform solution for I , with no evident dependencies on the radial distance from the Earth. We also note an inverse proportionality between the values of I and those of pitch angles. This is to be expected since for lower pitch angles, field line length between mirror points is greater

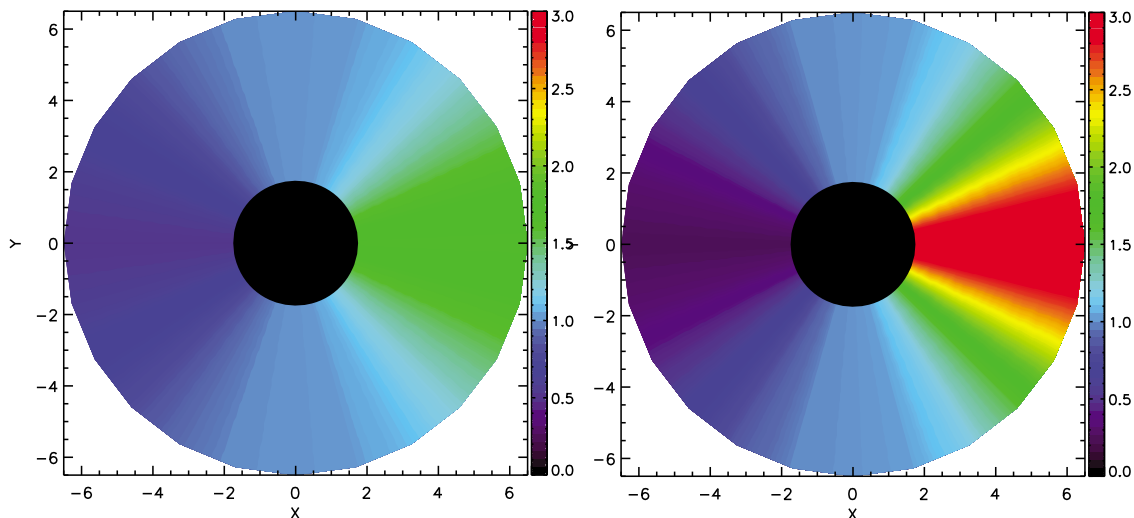


Figure 5. Dial plots of the ratios between the magnetic field magnitude of a dipole and the magnitude of the stretched field (left) with $a = 1.0$, $b = 0.1$ and (right) with $a = 1.0$, $b = 0.2$.

and therefore the integration is done over a larger domain. Nevertheless, the relative errors to the “analytical” solution are small (see Figure 3).

[38] For the case of a stretched dipole magnetic field, the configuration changes dramatically. For all pitch angles, the values of I on the dayside are significantly smaller than the values of I on the nightside. This is consistent with the fact that the magnetic field magnitude at these locations displays the exact opposite behavior (remember that I is proportional with the integral of $\sqrt{1 - \frac{B(s)}{B_m}}$ between the mirror points). As opposed to the case of a dipole where the values of I are relatively constant for a given pitch angle, in the cases of the stretched dipole, the values of I range over a larger domain for all pitch angles. Moreover, the I distributions show a dawn-dusk symmetry, which is to be expected due to the symmetry of the field at these locations as well as dipolar values for field lines close to the dawn and dusk. We also note that the more distorted the magnetic field, the larger are the differences between the I values on the nightside as opposed to the dayside.

[39] Similarly to Figure 7, Figure 8 shows the distribution of h values for a dipolar magnetic field configuration (Figures 8a, 8d, and 8g), an asymmetrically stretched dipole field with distortion factor $b = 0.1$ (Figures 8b, 8e, and 8h), and an asymmetrically stretched dipole field with distortion factor $b = 0.2$ (Figures 8c, 8f, and 8i) for the three choices of pitch angle described above. Again, for the dipole case and for a fixed pitch angle, the values are relatively constant and similar to the analytical solution. The gradients that are apparent in the solution for $\alpha_0 = 88^\circ$ are due to the oscillatory nature in the error from the integration on the end segments, near the mirror points. To understand the behavior of h we need to remember its definition (see equation (3)). So the profile of h would be given by the interplay between the two terms in the integrand. Although the term $\frac{1}{\sqrt{1 - \frac{B(s)}{B_m}}}$ is increasing with increasing magnetic field, the length of the field line between the mirror points has the opposite

behavior due to the field compression along the x axis. When the equatorial magnetic field becomes depressed, the distance between the mirror points can be shortened by the ring current in order to conserve the first adiabatic invariant. Just as in the case of I , h values for nearly equatorially mirroring particles span over a larger range for the same reasons explained above. For the case when the magnetic field is no longer dipolar, we note the day/night asymmetry as well as the symmetry in the dawn-dusk direction. This is consistent with the magnetic field configuration, with higher values of

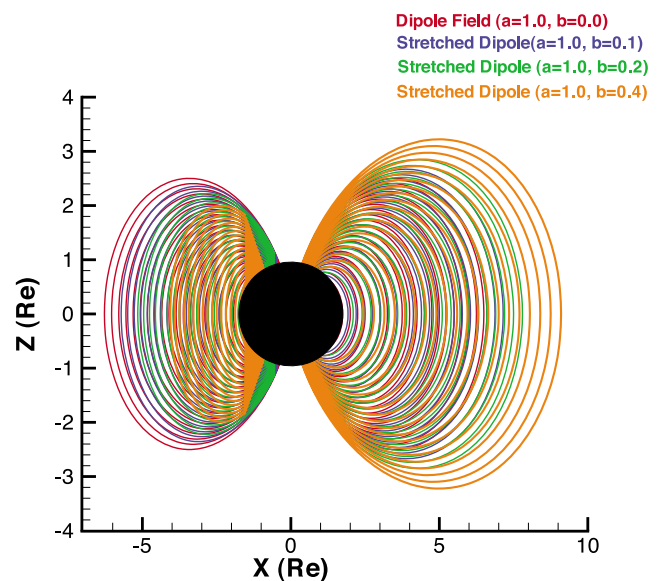


Figure 6. Magnetic field lines for various configurations of the magnetic field. Red lines show the dipole field lines, while blue, green, and orange lines show the asymmetrically stretched dipole field lines for $a = 1.0$ and $b = 0.1$, for $a = 1.0$ and $b = 0.2$, and for $a = 1.0$ and $b = 0.4$, respectively.

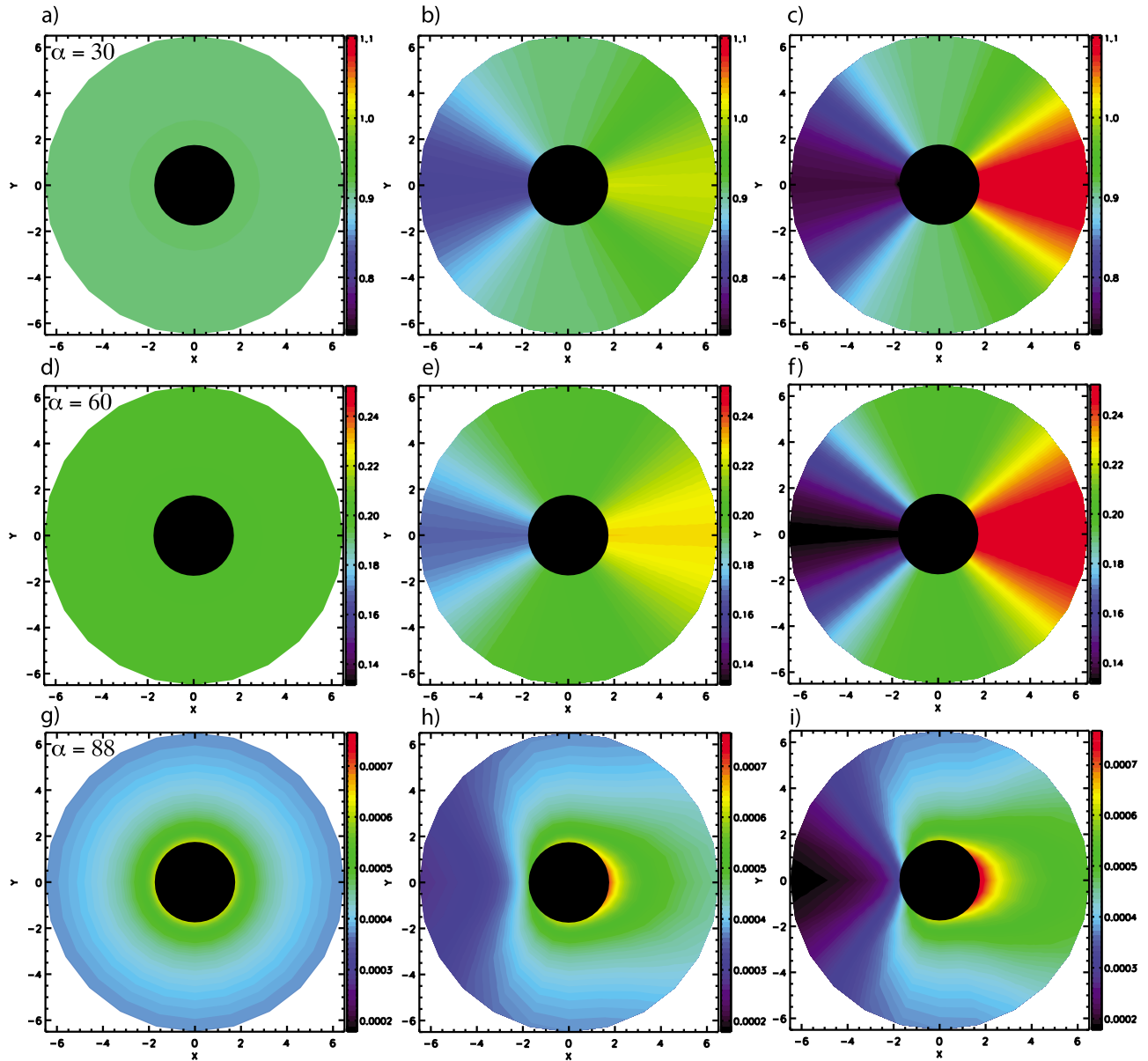


Figure 7. The distribution of I for (a, d, g) a dipole configuration, (b, e, h) a stretched dipole with $a = 1.0$ and $b = 0.1$, and (c, f, i) stretched dipole with $a = 1.0$ and $b = 0.2$. The results for three choices of pitch angles are 30° (Figures 7a–7c), 60° (Figures 7d–7f), and 88° (Figures 7g–7i).

the magnetic field magnitude yielding depressed values of the h parameter.

5. Results

5.1. Particle Drift Analysis

[40] To illustrate the profile of the bounce-averaged rate of change in the particle's energy, Figure 9 presents the distribution of $\langle \frac{dE}{dt} \rangle$ for a 107 keV energy particles moving in a dipole magnetic field (Figures 9a, 9d, and 9g), an asymmetrically stretched dipole field with distortion factor $b = 0.1$ (Figures 9b, 9e, and 9h), and an asymmetrically stretched dipole field with distortion factor $b = 0.2$ (Figures 9c, 9f, and 9i). Again, the $\langle \frac{dE}{dt} \rangle$ profiles are displayed for the three choices of pitch angle aforementioned.

[41] In the dipolar magnetic field case, the distribution of the bounce-averaged rate of change of the particles kinetic energy is only slightly varying with pitch angle. For example, for 30° pitch angle $\langle \frac{dE}{dt} \rangle$ varies between $[-7.6, 7.6]$, for 60° pitch angle $\langle \frac{dE}{dt} \rangle$ varies between $[-8.6, 8.6]$ while for 88° pitch angle $\langle \frac{dE}{dt} \rangle$ varies between $[-9.0, 9.0]$. Moreover, it displays dawn/dusk symmetry, with positive changes in the particles's energy on the nightside and negative changes on the dayside. In the case of a dipole field, $\langle \frac{dE}{dt} \rangle$ varies only with the particle's radial drift, which in this case is only provided by the convective drift. This also explains the symmetric distribution due to symmetric electric potential pattern provided by the Volland-Stern model (see Figure 10).

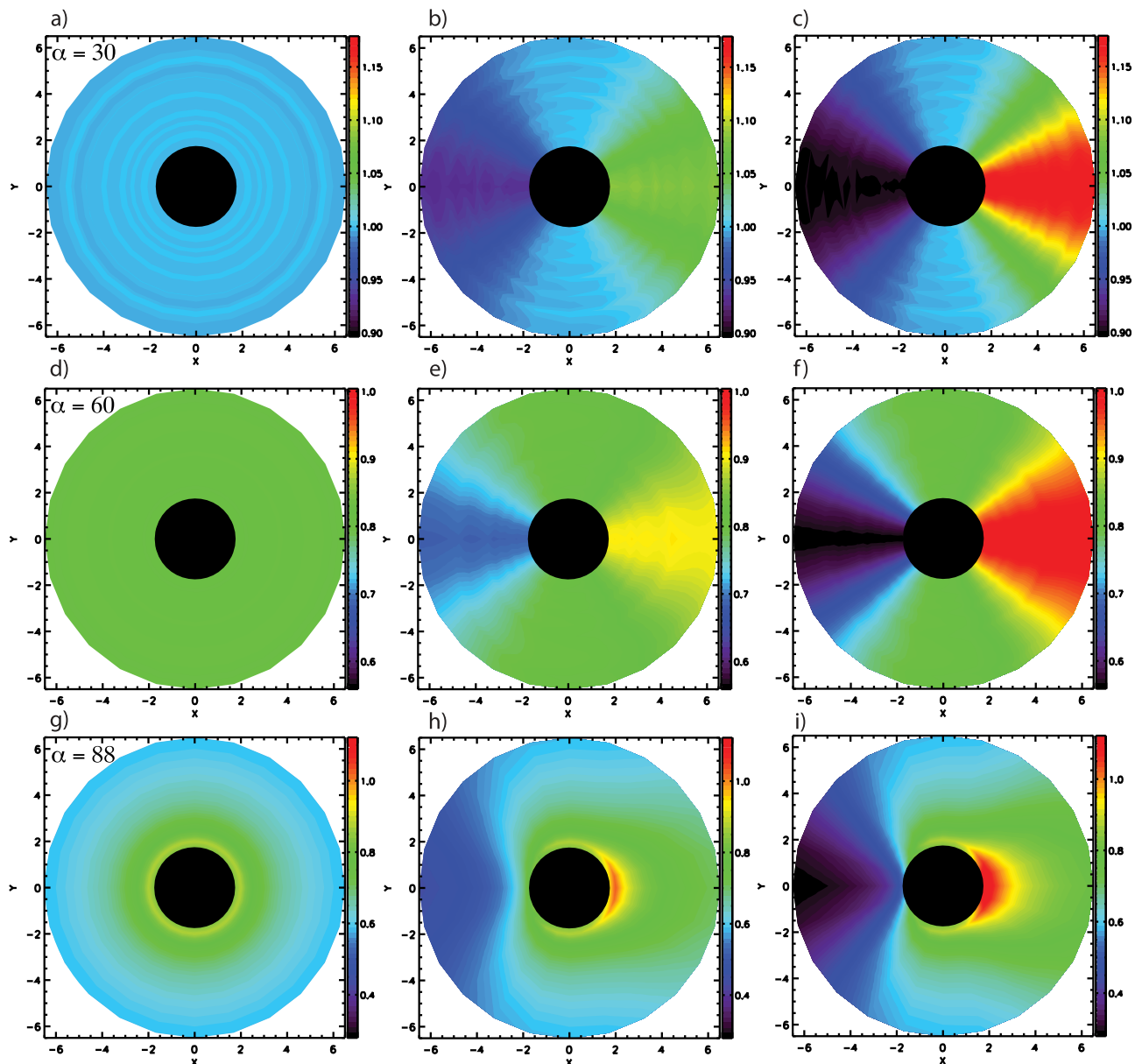


Figure 8. The distribution of h for (a, d, g) a dipole configuration, (b, e, h) a stretched dipole with $a = 1.0$ and $b = 0.1$, and (c, f, i) a stretched dipole with $a = 1.0$ and $b = 0.2$. The results for three choices of pitch angles are 30° (Figures 8a–8c), 60° (Figures 8d–8f), and 88° (Figures 8g–8i).

[42] When the magnetic field is distorted by a $b = 0.1$ distortion factor (Figures 9b, 9e, and 9h), the $\langle \frac{dE}{dt} \rangle$ distribution changes dramatically. A positive change in the particle's energy is seen in the evening sector (1800 LT–0000 LT quadrant) while the post dawn and the dayside regions are dominated by a negative change in energy. This is due to the change in the magnetic field, with a stronger field on the day side and dawn/dusk sides have the same values at the same radial distance as compared to the dipole field. This in turn changes the gradient curvature drift, altering the particles total radial drift. Fresh particles injected on the night side, now encounter a weaker magnetic field and drift faster toward the dayside. Moreover, the radial component of the gradient curvature drift is nonzero, therefore contributing to

the total radial drift. If for the dipole case, $\langle \frac{dE}{dt} \rangle$ varies in a range centered on 0.0, for the nondipole field, this is not the case. For instance, for a 30° equatorial pitch angle, $\langle \frac{dE}{dt} \rangle$ ranges from -5.9 to 15.3 .

[43] When distorting the field even more (Figure 9, right), larger peaks develop on the evening while in the postdawn sector the changes in the particles energy are depressed even more. We note that $\langle \frac{dE}{dt} \rangle$ not only is slightly changing shape but it increases in value with decreasing pitch angle. This is of course due to the longer bounce lengths, and therefore higher values of the integrals. Therefore, when the magnetic field departs from the dipolar configuration, the bounce-averaged rate of change in the particle's energy changes significantly, both in value and distribution.

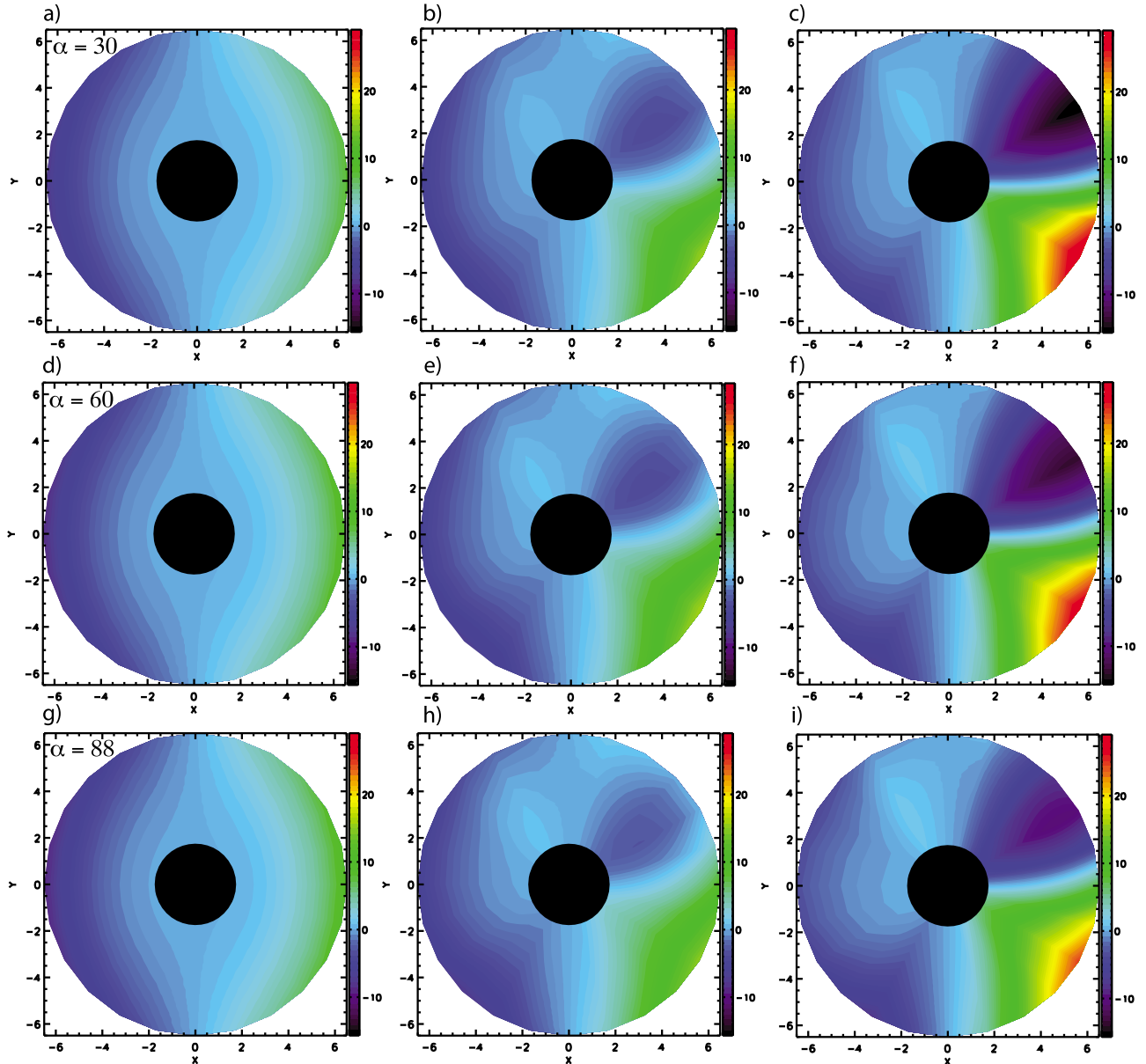


Figure 9. The distribution of $\langle \frac{dE}{dt} \rangle$ for (a, d, g) a dipole configuration, (b, e, h) a stretched dipole with $a = 1.0$ and $b = 0.1$, and (c, f, i) a stretched dipole with $a = 1.0$ and $b = 0.2$. The results for three choices of pitch angles are 30° (Figures 9a–9c), 60° (Figures 9d–9f), and 88° (Figures 9g–9i).

[44] Similarly to Figure 9, Figure 11 presents the distribution of $\langle \frac{d\mu_0}{dt} \rangle$ for 107 keV particles moving in a dipole configuration (Figures 11a, 11d, and 11g), along with the stretched dipole cases $b = 0.1$ (Figures 11b, 11e, and 11h) and $b = 0.2$ (Figures 11c, 11f, and 11i) for all three choices of pitch angle. For the dipole magnetic field, the change in the particles equatorial pitch angle seems to be constant at all radial distances. However, the value of $\langle \frac{d\mu_0}{dt} \rangle$ increases with decreasing pitch angle.

[45] The changes in the particle's equatorial pitch angles are more dramatic when the magnetic field is distorted. A peak in $\langle \frac{d\mu_0}{dt} \rangle$ develops on the evening sector, while a well

develops in the postdawn region, similarly to $\langle \frac{dE}{dt} \rangle$. We note that in the dawn and dusk regions the change in the particle's pitch angle is the same as in the dipole case, as expected.

[46] The variations in the $\langle \frac{d\mu_0}{dt} \rangle$ distribution are due to not only the change in the magnetic field strength but to the changes to the field line length between the mirror point. Furthermore, the distribution of $\langle \frac{d\mu_0}{dt} \rangle$ presents more pronounced wells on the nightside while new ones are appearing in the afternoon sector as the field becomes more distorted.

[47] Figure 12 shows the drift in the $\hat{\phi}$ (Figures 12a–12f) and \hat{r} (Figures 12g–12l) direction of a charged particle with kinetic energy 107 keV , moving in a dipolar magnetic field

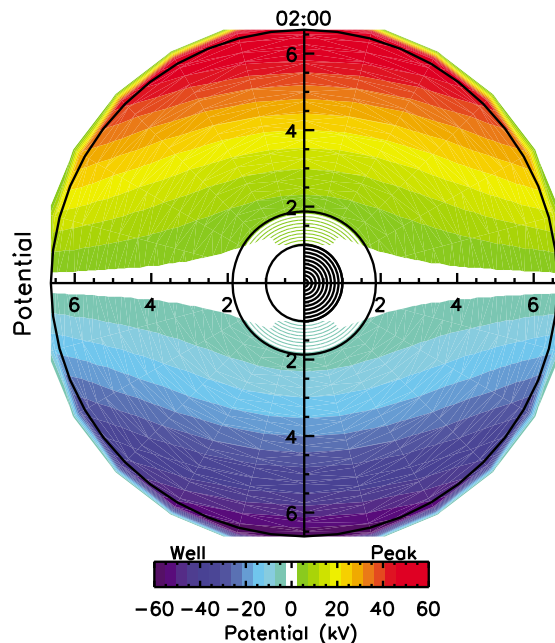


Figure 10. Convection electric potential contours generated by the Volland-Stern model. The view is over the northern hemisphere and the distances are expressed in Earth radii (R_e).

(black line) and the azimuthal (Figures 12a–12f) and radial (Figures 12g–12l) drift in a stretched dipole configuration with a distortion factor of $b = 0.1$ (blue line) and $b = 0.2$ (red line). Figure 12a shows the V_ϕ component of the gradient curvature drift for a nearly equatorially mirroring particle versus L shell at midnight, for all three cases, while Figure 12b shows the same parameter values extracted at noon local time. We note that when the magnetic field is compressed on the dayside, the gradient curvature drift in the $\hat{\phi}$ direction is decreasing (weakens) with increasing distortion factor. This is to be expected since the drift velocity goes as $\sim \frac{1}{B^2}$, therefore a particle in a compressed field will experience slower drifts relative to a dipolar magnetic field configuration. For instance at local midnight and at a radial distance of $5 R_e$ from the Earth, $\hat{\phi}$ component of the gradient curvature drift is increased by ~ 1.6 (~ 2.6) times when the magnetic field is distorted by $b = 0.1$ ($b = 0.2$) distortion factor. Moreover, the azimuthal drift on the dayside (at local noon) has the opposite behavior; at $5 R_e$ on the dayside, the percent difference between the dipolar gradient curvature V_ϕ and the stretched dipole with $b = 0.1$ ($b = 0.2$) is of about 184% (222%). Therefore, the azimuthal drifts are increasing with larger (weaker) distances (B fields) as expected.

[48] Figure 12c shows the variation of $\hat{\phi}$ component of the gradient curvature drift with the particles equatorial pitch angle for midnight local time, followed by the same quantities extracted at local noon (Figure 12d). Again, we note that the drifts are decreasing in magnitude with increasing compression of the magnetic field.

[49] Figure 12e presents the behavior of the gradient curvature V_ϕ as a function of local time. The azimuthal drift a particle experiences in a dipolar magnetic field is constant with local time due to the azimuthal symmetry of the dipolar

magnetic field. However, for a particle mirroring in the vicinity of the equatorial plane, the stretched dipole produces a magnetic drift in the $\hat{\phi}$ direction that is largest on the nightside, where the magnetic field is depressed and minimum on the dayside (noon) where the field has the maximum compression. Also, dawn and dusk drifts are the same as in the dipole case, as expected. The drift at both dawn and dusk for the distorted dipole fields have identical values to the drifts in a dipolar field (not shown here). Additionally, as we increase the compression on the dayside, the azimuthal drift approaches zero. Figure 12f presents the total $\hat{\phi}$ drift (including convection too). We note the contribution from the convective drift due to the Volland-Stern electric field, as the imposed sine wave pattern.

[50] In the case of the radial gradient curvature drift (see Figures 12g–12l), a particle moving in a more compressed magnetic field experiences a larger drift, that are also increasing with increasing radial distance from the Earth. Similar behavior is noted regarding the pitch angle dependency; the radial component of the gradient curvature drift shows increase with increasing compression. We also note that gradient curvature V_r as a function of magnetic local time (Figure 12l) has an oscillatory behavior, approaching zero at dawn and dusk (by construction of the magnetic field) and also at noon and midnight. Therefore, at these local times, the ring current particles experience only convection drifts, as it can be seen from Figure 12l, where the total radial drift is presented.

[51] An important conclusion can be drawn from Figures 12f and 12l. For the stretched dipole configurations selected for this study, the nondipolar magnetic drifts can be (at certain places) larger in magnitude than the convective drifts. For example, the maximum percent difference between the total azimuthal drift in a dipole magnetic field and in a stretched field with $b = 0.1$ ($b = 0.2$) is of about $\sim 183\%$ ($\sim 245\%$). Similarly, the maximum percent difference between the total radial drift in a dipole magnetic field and in a stretched field with $b = 0.1$ ($b = 0.2$) is of approximately $\sim 623\%$ ($\sim 872\%$) for high-energy ions. That is, the radial component of the gradient curvature drifts for a nondipolar field can completely overpower the radial convective drift. Therefore, under certain disturbed conditions, the distorted magnetic field would alter the gradient curvature drifts in such a way that they dominate the total particle drift.

5.2. Hot Ion Pressure Analysis

[52] As a final test, we conducted idealized input simulations with HEIDI involving all magnetic field configurations aforementioned. H^+ and O^+ are the only ring current ions considered for these simulations and the calculations start with an empty magnetosphere. The electron densities are set to be equal to the proton densities, however the electron temperature is lower by a factor of 7.8 [Baumjohann *et al.*, 1989]. The electric potential is given by the Kp driven Volland-Stern model [Volland, 1973; Stern, 1975]. Please note that for our experiment, the particles were injected on the nightside at a constant rate and the Kp index was set to the value 7 throughout the simulations.

[53] Figure 13a shows the pressure distribution in the equatorial plane for HEIDI with dipole field and Ejiri [1978] formulations for both the I and h integrals and

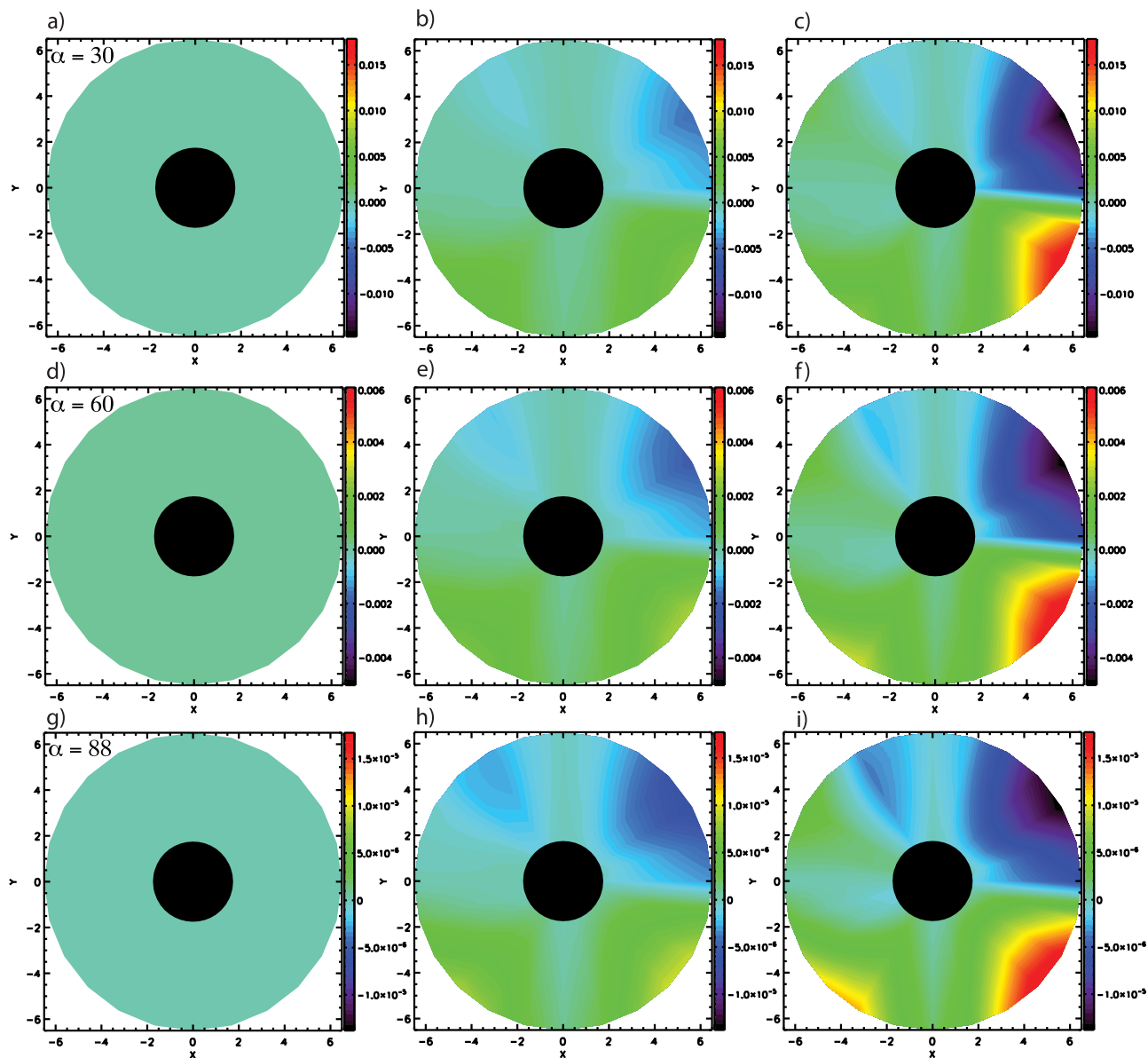


Figure 11. The distribution of $\langle \frac{d\mu_0}{dt} \rangle$ for (a, d, g) a dipole configuration, (b, e, h) a stretched dipole with $a = 1.0$ and $b = 0.1$, and (c, f, i) a stretched dipole with $a = 1.0$ and $b = 0.2$. The results for three choices of pitch angles are 30° (Figures 11a–11c), 60° (Figures 11d–11f), and 88° (Figures 11g–11i).

for the bounce-averaged coefficients (“Analytical Approximation”). Figure 13b shows the pressure distribution simulation results for HEIDI with dipole field, but this time obtained from HEIDI with a dipole field and the new formulations and numerical integrations for the bounce-averaged coefficients (“Numeric Integration”). Figures 13c and 13d show the pressure distribution in the equatorial plane obtained with HEIDI with a stretched dipole with $b = 0.1$ and $b = 0.2$ distortion factor, respectively. Each column presents pressure results at different times (4, 8, 12, 16, 20, 24 h) into the simulation.

[54] Comparing Figures 13a and 13b, the “Analytical Approximation” results versus the “Numeric Integration” results, we note that the latter produces lower pressures, although the topology remains the same. One reason for this is that the numerical integrals are underestimated due to the

fact that the algorithm we use to avoid the mirror point singularities assumes that the magnetic field varies linearly between two consecutive grid point. Although this assumption helps avoid this singularity and provides a good solution for a reasonable sized field aligned grid, it also shortens the field line length (as compared to the analytical solution). Therefore the values of the bounce-averaged coefficients as well as the values of I and h are underestimated. The differences between the peak pressures in those two cases are of the order of 20%. This might seem a high, however, the “analytic dipole” that uses the *Ejiri* [1978] formulae is not at all analytic. Rather, the *Ejiri* [1978] solutions are polynomial fits to numerical solutions of the same quantities. Moreover, the differences come from cumulative errors of less than 1% over 4000 time steps in all bounce-averaged quantities.

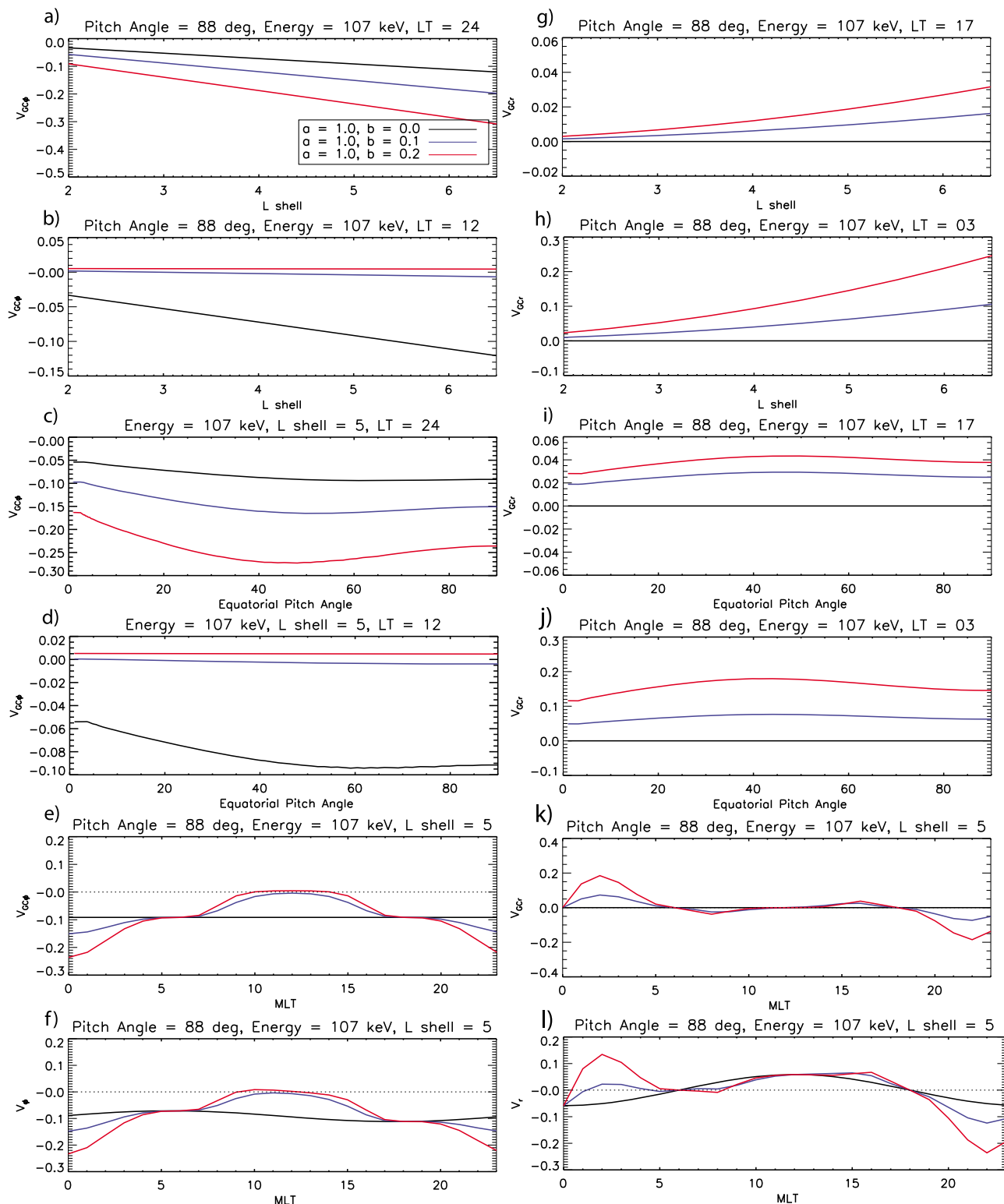


Figure 12. Particle drifts in the (left) $\hat{\phi}$ and (right) \hat{r} direction for a dipole (black lines) and the stretched dipole configuration with $b = 0.1$ (blue lines) and $b = 0.2$ (red lines). On the left, we present the $\hat{\phi}$ component of the gradient curvature drift versus L shell for (a) LT = 24 and (b) LT = 12, pitch angles for (c) LT = 24 and (d) LT = 12, and (e) local time. (f) The $\hat{\phi}$ component of the total particle drift is shown as a function of local time. On the right, we present the \hat{r} component of the gradient curvature drift versus L shell for (g) LT = 17 and (h) LT = 03, pitch angle for (i) LT = 17 and (j) LT = 03, and (k) local time. (l) The $\hat{\phi}$ component of the total particle drift is shown as a function of local time. Please note that the drift velocities are expressed in units of L shells/sec.

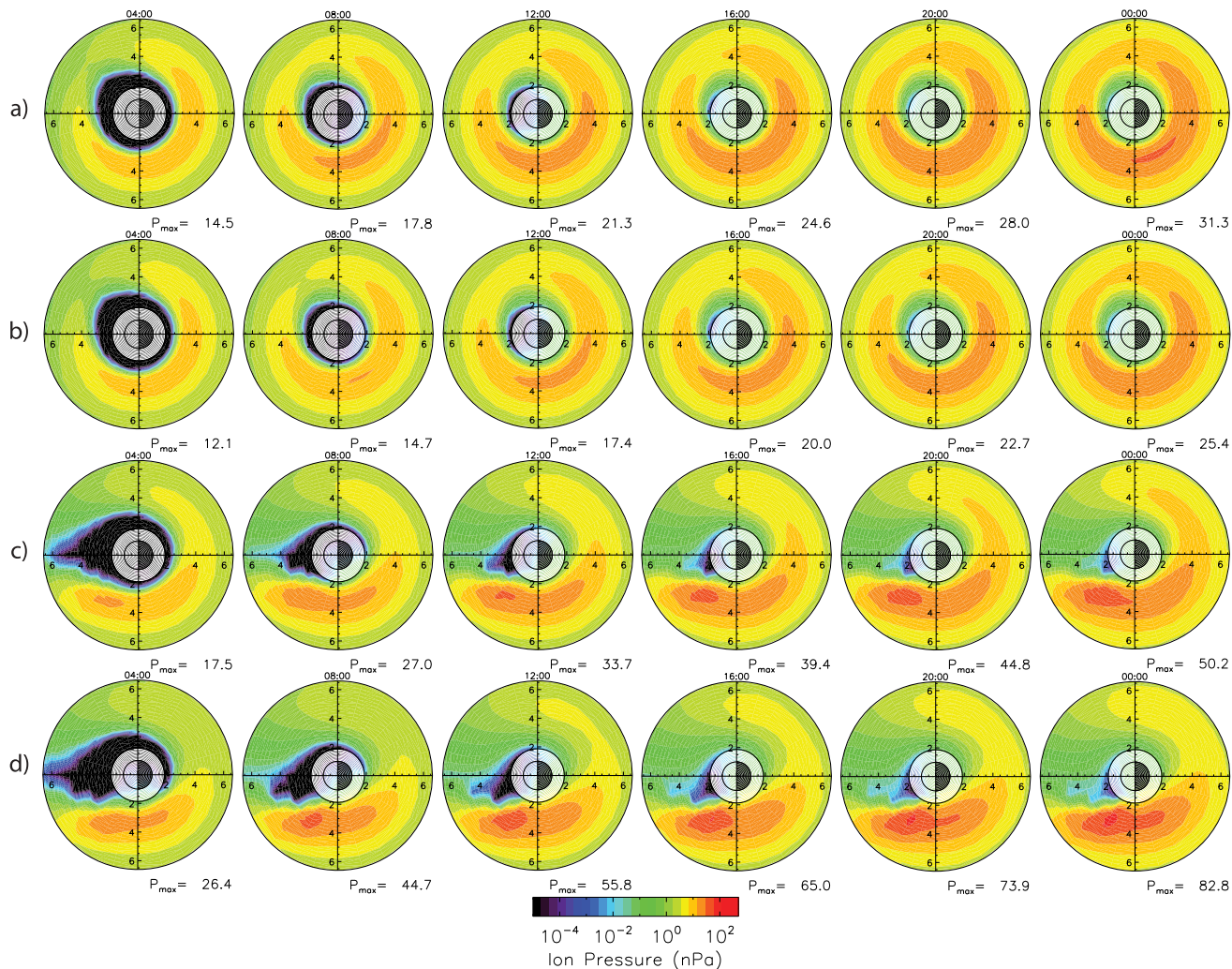


Figure 13. Pressure distribution in the equatorial plane for different model simulations. (a) The HEIDI results for the “Analytical Approximation” for a dipole field (*Ejiri* [1978] formulations for both the I and h integrals and for the bounce-averaged coefficients). (b) The HEIDI simulation results for the “Numerical Integration” (HEIDI with a dipole field and the new formulations and numerical integrations for the bounce-averaged coefficients), followed by the stretched dipole cases with (c) $b = 0.1$ and (d) $b = 0.2$. Each column presents a different time snapshot during each simulation.

[55] Figures 13c and 13d show the pressure distribution when the magnetic field is no longer dipolar. We note that a stretched dipole field configuration produces a significant increase in the buildup of the particle pressure during the first few hours of the simulation. This is because the changed fields modifies the particle drifts, increasing the drift speeds in regions of weaker magnetic field (nightside) and decreasing it in regions of stronger magnetic field (on the dayside). This will push particles from the nightside faster into the dayside, building up the pressure in this region and lowering the pressure on the nightside as compared to the dipole case. Moreover, the pressure stays on the duskside and does not wrap around the dayside as in the dipolar case. This is due to the fact that, for the two distorted magnetic field configurations examined, the gradient curvature drift slows down significantly on the dayside (see Figure 12). The total $\hat{\phi}$ drift stalls from about $LT = 9$ to $LT = 14$ and the flow

is mainly driven by the \hat{r} component of the total drift. Therefore the field compression on the dayside acts as a barrier to the flow of ring current particles. The asymmetry of the ring current pressure is dramatically increased due to the B field distortion.

[56] Figure 14 presents the variation of the maximum pressure during each of the simulations. The dotted black line shows the results from the “Analytical Approximation” run, black line corresponds to the pressure peaks values in the equatorial plane for the “Numeric Integration” run while the blue (red) line presents results from the run that used stretched dipole configuration with a distortion factor of $b = 0.1$ ($b = 0.2$). We note that in the first couple of hours of each simulation, the peak pressures are closer to each other, only to diverge more after 2 h. In Figure 14b, we see that, while for the dipole cases the peak pressure happens at more or less the same magnetic local time, when the magnetic field is

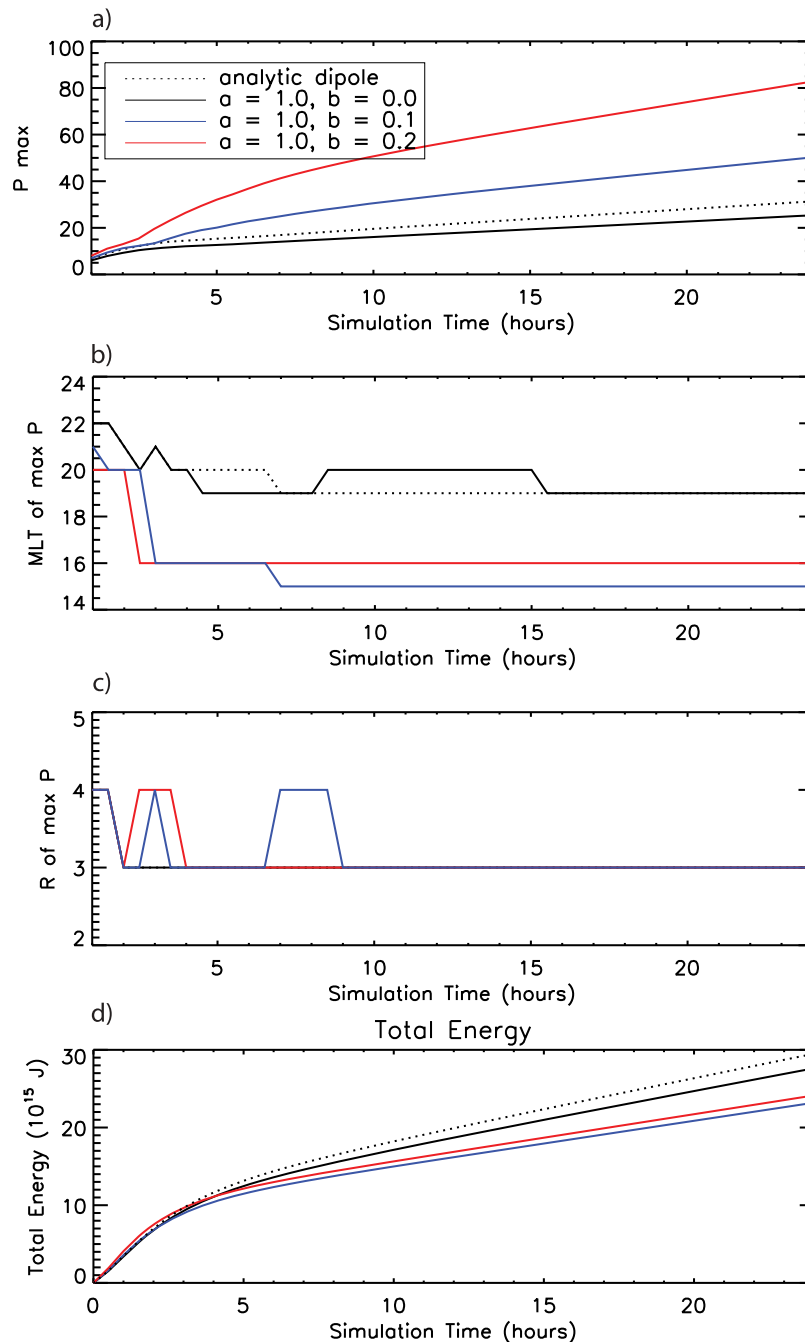


Figure 14. Pressure peaks evolution as a function of (a) simulation time, (b) magnetic local time, and (c) radial distance from the Earth. (d) The evolution of the total energy content during the simulation. The dotted black line shows the results from the “Analytical Approximation” run, the black line presents the results from the “Numeric Integration” run, and the blue (red) line shows results from stretched dipole with a distortion factor of $b = 0.1$ ($b = 0.2$) run.

highly distorted, the pressure peak moves to lower local times and stay there throughout the simulation. However, the radial distance varies with simulation time only during the first half of the simulation. After several hours, it remains at the same radial distance for all cases.

[57] Figure 14d presents the total energy content of the ring current for the three simulation setups. It is noted that in the case for which the magnetic field is dipolar, the total energy is the highest, a result consistent with the work of

Zaharia *et al.* [2006, 2008]. Lemon *et al.* [2004] and Liu *et al.* [2006] show that when the magnetic field is treated self-consistently, the developed ring current is weaker as compared to the dipole or dipole-like magnetic field models, producing a weaker disturbance of the geomagnetic field. Also, this magnetic field perturbation prevents the injection of a ring current particles closer to the Earth. Our results also support this findings.

[58] For the distorted dipole cases, the drifts on the night-side are consistently higher for the distorted dipole case, while much lower on the dayside. On the other hand, not only the nightside particle injection is constant (by construction), but it is the same for all simulations. In the nondipolar cases, more drift paths are open leading to larger drift-out loss and lower energy content in the inner magnetosphere.

6. Conclusions and Future Work

[59] We now have a new version of the Hot Ion Electron Drift Integrator model that is capable of accommodating arbitrary magnetic fields. A new formalism for the bounce-averaged coefficients has been developed, implemented and tested within HEIDI and the derivations of these bounce-averaged coefficients are presented for the first time. We show that during times of distorted magnetic field the change in particle's pitch angle and energy deviates greatly from the corresponding distribution as predicted by the dipolar *Ejiri* [1978] formulation. The bounce average change in the particles energy is no longer symmetrical as in the dipolar magnetic field case, but the new arbitrary magnetic field formulation allows for skewed distributions with new peaks and wells developing in regions of distorted magnetic field as a result of modified magnetic drifts. Also, the change in pitch angle is now anisotropic, showing minima and maxima that are local time dependent.

[60] We have found that changing the way the magnetic field is handled in HEIDI, changes the whole topology of the ring current. The drifts are altered due to distortion in the magnetic field, i.e., slower drifts on the dayside due to the field compression and increasingly higher magnetic drifts on nightside proportional to the magnetic field stretching. Therefore ring current ions are being moved faster from the nightside toward the dayside, where they start to slow down, building up the pressure in this region. We showed that under certain disturbed conditions, the nondipolar magnetic drifts can be dominate the total particle drift, significantly increasing the ring current ion pressure on the duskside. Therefore, the field compression on the dayside can act as a barrier to the flow of ring current ions, dramatically altering the pressure distribution in the equatorial plane and increasing the asymmetry of the ring current. Moreover, the timing of the pressure buildup is heavily dependent on the nature of the magnetospheric magnetic field.

[61] However, additional improvements are necessary for a more comprehensive model. Electric fields in the magnetosphere have both potential and inductive components. For instance, the inclusion of inductive electric fields that arise due to the time varying nature of the magnetic field are believed to play an important role in a realistic description of the convection. Previous models that included such fields [Fok and Moore, 1997] were based on ionospheric grids and used the assumption that the ionospheric foot point of the magnetic field is fixed in the ionosphere for the process of magnetic reconfiguration. Therefore a measure of the field displacement can be used as a proxy for the inductive component of the electric field. On the other hand, inclusion of inductive electric fields can be quite a challenging task when using equatorial based grids, since it requires a Biot Savart like integration over the whole domain. This will be achieved by full inclusion of this new nondipolar version of HEIDI

within the Space Weather Modeling Framework [Tóth *et al.*, 2006]. This coupling, and the new scientific studies it allows, will be the focus of a follow-up paper in the very near future.

Appendix A: Bounce-Averaged Coefficients

[62] For the interested reader, and for completeness, the derivation of the bounce-averaged coefficients for an arbitrary magnetic field is detailed below.

[63] In the presence of external forces which are perpendicular to the magnetic field lines at all times (equipotential field lines), the particle's momentum and the magnetic field at the mirror points are not conserved. However, the magnetic moment and the second adiabatic invariant remain constants. The bounce-averaged rate of change of the cosine of the particle's pitch angle at the magnetic equator is derived from the conservation of the magnetic moment μ_m

$$\mu_m = \frac{1}{2} \frac{mv_{\perp}^2}{B} = \frac{1}{2} \frac{mv^2 \sin^2 \alpha_0}{B_0} \quad (\text{A1})$$

and the second adiabatic invariant J

$$J = 2mv \int_{s_m}^{s_m'} ds \sqrt{1 - \frac{B(s)}{B_m}} \quad (\text{A2})$$

where B_0 represents the equatorial value of the magnetic field, $B(s)$ is the magnetic field along the field line, s is the distance from the ionospheric foot point along the field line, B_m denotes the magnitude of the magnetic field at the mirror points s_m and s_m' and v is the particle's velocity. The velocity of the particle can be eliminated by combining the two invariants:

$$\frac{\mu_m}{J^2} = \text{constant} \quad (\text{A3})$$

Letting $y = \sin \alpha_0$ yields:

$$\frac{\mu_m}{J^2} = \frac{y^2}{8mB_0 I^2 R_0^2} \quad (\text{A4})$$

Furthermore, differentiating (A4) with respect to time we get:

$$\frac{2}{y} \frac{dy}{dt} - \frac{1}{B_0} \frac{dB_0}{dt} - \frac{2}{R_0} \frac{dR_0}{dt} - \frac{2}{I} \frac{dI}{dt} = 0 \quad (\text{A5})$$

Equation (A1) along with energy conservation yields a relationship between the magnetic field at the mirror point (B_m), magnetic field at the equator (B_0) and the particle's equatorial pitch angle (α_0):

$$B_m = \frac{B_0}{\sin^2 \alpha_0} \quad (\text{A6})$$

Therefore, using the expressions of I (equation (5)) and h (equation (3)) together with equation (A6) we can rewrite these expressions as below:

$$I = \frac{1}{R_0} \int_{s_m}^{s_m'} ds \sqrt{1 - \frac{B(s)y^2}{B_0}} \quad (\text{A7})$$

and

$$h = \frac{1}{2R_0} \int_{s_m}^{s_m'} \frac{ds}{\sqrt{1 - \frac{B(s)y^2}{B_0}}} \quad (\text{A8})$$

However, the last term in equation (A5) ($\frac{dl}{dt}$) needs further examination and differentiating (A7) we can express $\frac{dl}{dt}$ as:

$$\frac{dl}{dt} = \left(\frac{1}{R_0} \sqrt{1 - \frac{B(s_m)y^2}{B_0}} \right) \frac{ds_m'}{dt} - \left(\frac{1}{R_0} \sqrt{1 - \frac{B(s_m)y^2}{B_0}} \right) \frac{ds_m}{dt} + \int_{s_m}^{s_m'} \frac{\partial}{\partial t} \frac{1}{R_0 \sqrt{1 - \frac{B(s)y^2}{B_0}}} ds \quad (\text{A9})$$

We can easily show that the first two terms on the right-hand side of the equation above are zero.

$$\left(\frac{1}{R_0} \sqrt{1 - \frac{B(s_m')y^2}{B_0}} \right) \frac{ds_m'}{dt} = \left(\frac{1}{R_0} \sqrt{1 - \frac{B(s_m)y^2}{B_0}} \right) \frac{ds_m}{dt} = \frac{1}{R_0} \sqrt{1 - \frac{B_m y^2}{B_0}} = 0 \quad (\text{A10})$$

Therefore, $\frac{dl}{dt}$ becomes:

$$\frac{dl}{dt} = \int_{s_m}^{s_m'} \frac{\partial}{\partial t} \frac{1}{R_0 \sqrt{1 - \frac{B(s)y^2}{B_0}}} ds = \frac{\partial I}{\partial t} + \frac{\partial I}{\partial y} \frac{\partial y}{\partial t} + \frac{\partial I}{\partial R_0} \frac{\partial R_0}{\partial t} + \frac{\partial I}{\partial \phi} \frac{\partial \phi}{\partial t} \quad (\text{A11})$$

The second term in equation (A11) can be further simplified by solving for $\frac{d}{dy} \left(\frac{I}{y} \right)$ first and then relating the $\frac{\partial I}{\partial y}$ term with I and h quantities.

$$\frac{\partial}{\partial y} \left(\frac{I}{y} \right) = -\frac{I}{y^2} + \frac{1}{y} \frac{\partial I}{\partial y} \quad (\text{A12})$$

$$\frac{\partial I}{\partial y} = \frac{1}{R_0} \int_{s_m}^{s_m'} -\frac{B(s)y}{B_0} \frac{ds}{\sqrt{1 - \frac{B(s)y^2}{B_0}}} \quad (\text{A13})$$

$$\frac{\partial}{\partial y} \left(\frac{I}{y} \right) = -\frac{1}{R_0 y^2} \left(\int_{s_m}^{s_m'} ds \sqrt{1 - \frac{B(s)y^2}{B_0}} + y \int_{s_m}^{s_m'} \frac{B(s)y}{B_0} \frac{ds}{\sqrt{1 - \frac{B(s)y^2}{B_0}}} \right) \quad (\text{A14})$$

$$\frac{\partial}{\partial y} \left(\frac{I}{y} \right) = -\frac{1}{R_0 y^2} \int_{s_m}^{s_m'} \frac{ds}{\sqrt{1 - \frac{B(s)y^2}{B_0}}} \quad (\text{A15})$$

So we obtain

$$\frac{\partial}{\partial y} \frac{I}{y} = -\frac{2h}{y^2} \quad (\text{A16})$$

From equation (A12) and equation (A16) we get

$$\frac{\partial I}{\partial y} = \frac{I - 2h}{y} \quad (\text{A17})$$

Therefore, equation (A11) becomes:

$$\frac{dl}{dt} = \frac{\partial I}{\partial t} + \frac{(I - 2h)}{y} \frac{\partial y}{\partial t} + \frac{\partial I}{\partial R_0} \frac{\partial R_0}{\partial t} + \frac{\partial I}{\partial \phi} \frac{\partial \phi}{\partial t} \quad (\text{A18})$$

Now, we evaluate the third term ($\frac{\partial I}{\partial R_0} \frac{\partial R_0}{\partial t}$) in equation (A11).

$$\frac{\partial I}{\partial R_0} \frac{\partial R_0}{\partial t} = -\frac{1}{R_0^2} \frac{\partial R_0}{\partial t} \int_{s_m}^{s_m'} ds \sqrt{1 - \frac{B(s)y^2}{B_0}} + \frac{1}{R_0} \frac{\partial R_0}{\partial t} \int_{s_m}^{s_m'} \frac{\partial}{\partial R_0} \sqrt{1 - \frac{B(s)y^2}{B_0}} ds \quad (\text{A19})$$

$$\begin{aligned} \frac{\partial I}{\partial R_0} \frac{\partial R_0}{\partial t} &= -\frac{I}{R_0} \frac{\partial R_0}{\partial t} + \frac{1}{2R_0 B_0} \frac{\partial B_0}{\partial R_0} \frac{\partial R_0}{\partial t} \\ &\cdot \left(\int_{s_m}^{s_m'} \frac{ds}{\sqrt{1 - \frac{B(s)y^2}{B_0}}} - \int_{s_m}^{s_m'} ds \sqrt{1 - \frac{B(s)y^2}{B_0}} \right) \\ &+ \frac{1}{R_0} \frac{\partial R_0}{\partial t} \int_{s_m}^{s_m'} \sqrt{1 - \frac{B(s)y^2}{B_0}} \frac{\partial(ds)}{\partial R_0} - \frac{y^2}{2R_0 B_0} \frac{\partial R_0}{\partial t} \int_{s_m}^{s_m'} \\ &\cdot ds \frac{\frac{\partial B}{\partial R_0}}{\sqrt{1 - \frac{B(s)y^2}{B_0}}} \quad (\text{A20}) \end{aligned}$$

$$\begin{aligned} \frac{\partial I}{\partial R_0} \frac{\partial R_0}{\partial t} &= \frac{\partial R_0}{\partial t} \left(-\frac{I}{R_0} + \frac{(2h - I)}{2B_0} \frac{\partial B_0}{\partial R_0} + \frac{1}{R_0} \int_{s_m}^{s_m'} \right. \\ &\cdot \left. \sqrt{1 - \frac{B(s)y^2}{B_0}} \frac{\partial(ds)}{\partial R_0} - \frac{y^2 S_B}{2R_0 B_0} \left\langle \frac{\partial B}{\partial R_0} \right\rangle \right) \quad (\text{A21}) \end{aligned}$$

In the case of a dipolar magnetic field it can be shown that the $\frac{\partial I}{\partial R_0} = 0$ as well as $\frac{\partial I}{\partial \phi} \frac{\partial \phi}{\partial t} = 0$ and $\frac{\partial I}{\partial t} = 0$.

[64] Returning to equation (A5) and solving for $\frac{dy}{dt}$ using equation (A18), this yields:

$$\frac{dy}{dt} = \frac{y}{2} \left(\frac{1}{B_0} \frac{dB_0}{dt} + \frac{2}{R_0} \frac{R_0}{dt} - \frac{2}{I} \frac{dI}{dt} \right) \quad (\text{A22})$$

$$\frac{dy}{dt} = \frac{Iy}{2h} \left(\frac{1}{2B_0} \frac{dB_0}{dt} + \frac{1}{R_0} \frac{dR_0}{dt} + \frac{1}{I} \frac{\partial I}{\partial t} + \frac{1}{I} \frac{\partial I}{\partial R_0} \frac{\partial R_0}{\partial t} + \frac{1}{I} \frac{\partial I}{\partial \phi} \frac{\partial \phi}{\partial t} \right) \quad (\text{A23})$$

Please note that in our model R_0 , ϕ_0 , E , α_0 are independent variables, therefore $\frac{dy}{dt} = \frac{\partial y}{\partial t}$ as well as $\frac{dR_0}{dt} = \frac{\partial R_0}{\partial t}$.

[65] Considering that B_0 is a function $B_0(t, R_0, \phi)$, the total derivative $\frac{dB_0}{dt}$ becomes:

$$\frac{dB_0}{dt} = \frac{\partial B_0}{\partial t} + \frac{\partial B_0}{\partial R_0} \frac{\partial R_0}{\partial t} + \frac{\partial B_0}{\partial \phi} \frac{\partial \phi}{\partial t} \quad (\text{A24})$$

The total velocity vector in the equatorial plane in spherical coordinates,

$$\vec{v}_0 = \hat{R}_0 \frac{\partial R_0}{\partial t} + \hat{\phi}_0 \frac{\partial \phi}{\partial t} \quad (\text{A25})$$

has its components defined as:

$$v_{0R} = \frac{\partial R_0}{\partial t} = \left\{ \frac{m_t}{qB_0^4} \left(v_{\parallel}^2 + \frac{v_{\perp}^2}{2} \right) \left[\left(\nabla \frac{B_0^2}{2} \right) \times \vec{B}_0 \right] + v_{convection} \right\} \hat{R}_0 \quad (\text{A26})$$

$$v_{0\phi} = R_0 \frac{\partial \phi}{\partial t} = \left\{ \frac{m_t}{qB_0^4} \left(v_{\parallel}^2 + \frac{v_{\perp}^2}{2} \right) \left[\left(\nabla \frac{B_0^2}{2} \right) \times \vec{B}_0 \right] + v_{corotation} \right\} \hat{\phi} \quad (\text{A27})$$

Going back in equation (A23), we are able to obtain an expression for $\frac{dy}{dt}$ as a function of I , h , B_0 field magnitude and total drift components v_{0R} and $v_{0\phi}$:

$$\frac{dy}{dt} = \frac{Iy}{2h} \left\{ v_{0R} \left(\frac{1}{2B_0} \frac{\partial B_0}{\partial R_0} + \frac{1}{R_0} + \frac{1}{I} \frac{\partial I}{\partial R_0} \right) + v_{0\phi} \left(\frac{1}{2B_0 R_0} \frac{\partial B_0}{\partial h} + \frac{1}{IR_0} \frac{\partial I}{\partial \phi} \right) + \frac{1}{2B_0} \frac{\partial B_0}{\partial t} + \frac{1}{I} \frac{\partial I}{\partial t} \right\} \quad (\text{A28})$$

Transforming $\mu_0 = \sqrt{1 - y^2}$ and taking into account that in the case of no parallel electric fields, we have:

$$\left\langle \frac{d\mu_0}{dt} \right\rangle = - \frac{(1 - \mu_0^2)I}{2h\mu_0} \left\{ v_{0R} \left(\frac{1}{2B_0} (\nabla B_0)_{\hat{R}_0} + \frac{1}{R_0} + \frac{1}{I} (\nabla I)_{\hat{R}_0} \right) + v_{0\phi} \left(\frac{1}{2B_0} (\nabla B_0)_{\hat{\phi}} + \frac{1}{I} (\nabla I)_{\hat{\phi}} \right) + \frac{1}{2B_0} \frac{\partial B_0}{\partial t} + \frac{1}{I} \frac{\partial I}{\partial t} \right\} \quad (\text{A29})$$

Additionally, the bounce-averaged rate of change of the kinetic energy of the particle is derived from the conservation of the first adiabatic invariant:

$$\frac{d}{dt} \left(\frac{1}{2} \frac{mv_{\perp}^2}{B} \right) = \frac{d}{dt} \left(\frac{E y^2}{B_0} \right) = 0 \quad (\text{A30})$$

$$\frac{dE}{dt} = \frac{E}{B_0} \frac{dB_0}{dt} - \frac{2E}{y} \frac{dy}{dt} \quad (\text{A31})$$

Substituting $\frac{dy}{dt}$ and $\frac{dB_0}{dt}$ in the expression for $\frac{dE}{dt}$, equation (A31) becomes:

$$\begin{aligned} \frac{dE}{dt} = & \frac{E}{B_0} \left(1 - \frac{I}{2h} \right) \frac{\partial B_0}{\partial t} + E v_{0R} \left(\frac{1}{B_0} \left(1 - \frac{I}{2h} \right) \frac{\partial B_0}{\partial R_0} \right. \\ & \left. - \frac{1}{h} \left(\frac{I}{R_0} + \frac{\partial I}{\partial R_0} \right) \right) + E v_{0\phi} \left(\frac{1}{B_0} \left(1 - \frac{I}{2h} \right) \frac{1}{R_0} \frac{\partial B_0}{\partial \phi} \right. \\ & \left. - \frac{1}{h R_0} \frac{\partial I}{\partial \phi} \right) - \frac{E}{h} \frac{\partial I}{\partial t} \end{aligned} \quad (\text{A32})$$

Again, bounce-averaging, for the case of no parallel electric fields, we obtain:

$$\begin{aligned} \left\langle \frac{dE}{dt} \right\rangle = & \frac{E}{B_0} \left(1 - \frac{I}{2h} \right) \frac{\partial B_0}{\partial t} + E v_{0R} \left(\frac{1}{B_0} \left(1 - \frac{I}{2h} \right) (\nabla B_0)_{\hat{R}_0} \right. \\ & \left. - \frac{1}{h} \left(\frac{I}{R_0} + (\nabla I)_{R_0} \right) \right) + E v_{0\phi} \left(\frac{1}{B_0} \left(1 - \frac{I}{2h} \right) (\nabla B_0)_{\hat{\phi}} \right. \\ & \left. - \frac{1}{h} (\nabla I)_{\hat{\phi}} \right) - \frac{E}{h} \frac{\partial I}{\partial t} \end{aligned} \quad (\text{A33})$$

The expressions for $\left\langle \frac{d\mu_0}{dt} \right\rangle$ and $\left\langle \frac{dE}{dt} \right\rangle$ derived above are valid for any magnetic field configuration.

[66] **Acknowledgments.** Work at Los Alamos was performed under the auspices of the U.S. Department of Energy with financial support from NFS grant IAA 1027008. Funding for this study was also provided by NASA grants NNX08AQ15G and NNX09AF45G and NSF grant ATM-0802705.

[67] Masaki Fujimoto thanks the reviewers for their assistance in evaluating this paper.

References

- Baumjohann, W., G. Paschmann, and C. A. Cattell (1989), Average plasma properties in the central plasma sheet, *J. Geophys. Res.*, *94*, 6597–6606, doi:10.1029/JA094iA06p06597.
- Brandt, P. C., D. G. Mitchell, Y. Ebihara, B. R. Sandel, E. C. Roelof, J. L. Burch, and R. Demajistre (2002), Global IMAGE/HENA observations of the ring current: Examples of rapid response to IMF and ring current-plasmasphere interaction, *J. Geophys. Res.*, *107*(A11), 1359, doi:10.1029/2001JA000084.
- Chen, M. W., M. Schulz, and L. R. Lyons (1993), Energy content of storm-time ring current from phase space mapping simulations, *Geophys. Res. Lett.*, *20*, 1727–1730, doi:10.1029/93GL01252.
- Chen, M. W., S. Liu, M. Schulz, J. L. Roeder, and L. R. Lyons (2006), Magnetically self-consistent ring current simulations during the 19 October 1998 storm, *J. Geophys. Res.*, *111*, A11S15, doi:10.1029/2006JA011620.
- De Zeeuw, D. L., S. Sazykin, R. A. Wolf, T. I. Gombosi, A. J. Ridley, and G. Toth (2004), Coupling of a global MHD code and an inner magnetospheric model: Initial results, *J. Geophys. Res.*, *109*, A12219, doi:10.1029/2003JA010366.
- Ebihara, Y., and M. Ejiri (2000), Simulation study on fundamental properties of the storm-time ring current, *J. Geophys. Res.*, *105*, 15,843–15,860, doi:10.1029/1999JA900493.
- Ebihara, Y., M.-C. Fok, R. A. Wolf, M. F. Thomsen, and T. E. Moore (2005), Nonlinear impact of plasma sheet density on the storm-time ring current, *J. Geophys. Res.*, *110*, A02208, doi:10.1029/2004JA010435.
- Ejiri, M. (1978), Trajectory traces of charged particles in the magnetosphere, *J. Geophys. Res.*, *83*, 4798–4810, doi:10.1029/JA083iA10p04798.
- Fok, M., and T. E. Moore (1997), Ring current modeling in a realistic magnetic field configuration, *Geophys. Res. Lett.*, *24*, 1775–1778, doi:10.1029/97GL01255.
- Fok, M., J. U. Kozyra, A. F. Nagy, C. E. Rasmussen, and G. V. Khazanov (1993), Decay of equatorial ring current ions and associated aeronomical consequences, *J. Geophys. Res.*, *98*, 19,381–19,393, doi:10.1029/93JA01848.
- Fok, M., R. A. Wolf, R. W. Spiro, and T. E. Moore (2001), Comprehensive computational model of Earth's ring current, *J. Geophys. Res.*, *106*, 8417–8424, doi:10.1029/2000JA000235.
- Ganushkina, N. Y., and T. I. Pulkkinen (2002), Particle tracing in the Earth's magnetosphere and the ring current formation during storm times, *Adv. Space Res.*, *30*, 1817–1820, doi:10.1016/S0273-1177(02)00455-6.
- Ganushkina, N. Y., T. I. Pulkkinen, V. F. Bashkurov, D. N. Baker, and X. Li (2001), Formation of intense nose structures, *Geophys. Res. Lett.*, *28*, 491–494, doi:10.1029/2000GL011955.
- Ganushkina, N. Y., T. I. Pulkkinen, A. Milillo, and M. Liemohn (2006), Evolution of the proton ring current energy distribution during 21–25 April 2001 storm, *J. Geophys. Res.*, *111*, A11S08, doi:10.1029/2006JA011609.
- Ilie, R., M. W. Liemohn, J. Borovsky, and J. Kozyra (2010a), An investigation of the magnetosphere-ionosphere response to real and idealized co-rotating interaction region events through global magnetohydrodynamic simulations, *Proc. R. Soc. A*, *466*, 3279–3303, doi:10.1098/rspa.2010.0074.
- Ilie, R., M. W. Liemohn, and A. Ridley (2010b), The effect of smoothed solar wind inputs on global modeling results, *J. Geophys. Res.*, *115*, A01213, doi:10.1029/2009JA014443.
- Jordanova, V. K., L. M. Kistler, J. U. Kozyra, G. V. Khazanov, and A. F. Nagy (1996), Collisional losses of ring current ions, *J. Geophys. Res.*, *101*, 111–126, doi:10.1029/95JA02000.
- Jordanova, V. K., Y. S. Miyoshi, S. Zaharia, M. F. Thomsen, G. D. Reeves, D. S. Evans, C. G. Moukikis, and J. F. Fennell (2006), Kinetic simulations of ring current evolution during the Geospace Environment Modeling challenge events, *J. Geophys. Res.*, *111*, A11S10, doi:10.1029/2006JA011644.
- Jorgensen, A. M., H. E. Spence, W. J. Hughes, and H. J. Singer (2004), A statistical study of the global structure of the ring current, *J. Geophys. Res.*, *109*, A12204, doi:10.1029/2003JA010090.

- Kim, H., and A. A. Chan (1997), Fully adiabatic changes in storm time relativistic electron fluxes, *J. Geophys. Res.*, *102*, 22,107–22,116, doi:10.1029/97JA01814.
- Kozyra, J. U., and M. W. Liemohn (2003), Ring current energy input and decay, *Space Sci. Rev.*, *109*, 105–131, doi:10.1023/B:SPAC.0000007516.10433.ad.
- Kozyra, J. U., M. W. Liemohn, C. R. Clauer, A. J. Ridley, M. F. Thomsen, J. E. Borovsky, J. L. Roeder, V. K. Jordanova, and W. D. Gonzalez (2002), Multistep *Dst* development and ring current composition changes during the 4–6 June 1991 magnetic storm, *J. Geophys. Res.*, *107*(A8), 1224, doi:10.1029/2001JA000023.
- Le, G., C. Russell, and K. Takahashi (2004), Morphology of the ring current derived from magnetic field observations, *Ann. Geophys.*, *22*, 1267–1295.
- Lemon, C., R. A. Wolf, T. W. Hill, S. Sazykin, R. W. Spiro, F. R. Toffoletto, J. Birn, and M. Hesse (2004), Magnetic storm ring current injection modeled with the Rice Convection Model and a self-consistent magnetic field, *Geophys. Res. Lett.*, *31*, L21801, doi:10.1029/2004GL020914.
- Liemohn, M. W., and P. C. Brandt (2005), Small-scale structure in the storm-time ring current, in *Inner Magnetosphere Interactions: New Perspectives From Imaging*, *Geophys. Monogr. Ser.*, vol. 159, edited by J. Burch, M. Schulz, and H. Spence, pp. 167–177, AGU, Washington, D. C.
- Liemohn, M. W., and J. U. Kozyra (2005), Testing the hypothesis that charge exchange can cause a two-phase decay, in *The Inner Magnetosphere: Physics and Modeling*, *Geophys. Monogr. Ser.*, vol. 155, edited by T. I. Pulkkinen, N. A. Tsyganenko, and R. H. W. Friedel, pp. 211–225, AGU, Washington, D. C., doi:10.1029/155GM23.
- Liemohn, M. W., J. U. Kozyra, V. K. Jordanova, G. V. Khazanov, M. F. Thomsen, and T. E. Cayton (1999), Analysis of early phase ring current recovery mechanisms during geomagnetic storms, *Geophys. Res. Lett.*, *26*, 2845–2848, doi:10.1029/1999GL900611.
- Liemohn, M. W., J. U. Kozyra, M. F. Thomsen, J. L. Roeder, G. Lu, J. E. Borovsky, and T. E. Cayton (2001), Dominant role of the asymmetric ring current in producing the stormtime *Dst**, *J. Geophys. Res.*, *106*, 10,883–10,904, doi:10.1029/2000JA000326.
- Liemohn, M. W., A. J. Ridley, D. L. Gallagher, D. M. Ober, and J. U. Kozyra (2004), Dependence of plasmaspheric morphology on the electric field description during the recovery phase of the 17 April 2002 magnetic storm, *J. Geophys. Res.*, *109*, A03209, doi:10.1029/2003JA010304.
- Liemohn, M. W., A. J. Ridley, P. C. Brandt, D. L. Gallagher, J. U. Kozyra, D. M. Ober, D. G. Mitchell, E. C. Roelof, and R. DeMajistre (2005), Parametric analysis of nightside conductance effects on inner magnetospheric dynamics for the 17 April 2002 storm, *J. Geophys. Res.*, *110*, A12S22, doi:10.1029/2005JA011109.
- Liemohn, M. W., A. J. Ridley, J. U. Kozyra, D. L. Gallagher, M. F. Thomsen, M. G. Henderson, M. H. Denton, P. C. Brandt, and J. Goldstein (2006), Analyzing electric field morphology through data-model comparisons of the Geospace Environment Modeling Inner Magnetosphere/Storm Assessment Challenge events, *J. Geophys. Res.*, *111*, A11S11, doi:10.1029/2006JA011700.
- Liu, S., M. W. Chen, M. Schulz, and L. R. Lyons (2006), Initial simulation results of storm-time ring current in a self-consistent magnetic field model, *J. Geophys. Res.*, *111*, A04225, doi:10.1029/2005JA011194.
- Lui, A. T. Y. (2003), Inner magnetospheric plasma pressure distribution and its local time asymmetry, *Geophys. Res. Lett.*, *30*(16), 1846, doi:10.1029/2003GL017596.
- Maynard, N. C., and A. J. Chen (1975), Isolated cold plasma regions: Observations and their relation to possible production mechanisms, *J. Geophys. Res.*, *80*, 1009–1013, doi:10.1029/JA080i007p01009.
- McIlwain, C. E. (1986), A K_p dependent equatorial electric field model, *Adv. Space Res.*, *6*(3), 187–197, doi:10.1016/0273-1177(86)90331-5.
- Nakamura, R., K. Kamei, Y. Kamide, D. N. Baker, J. B. Blake, and M. Looper (1998), SAMPEX observations of storm-associated electron flux variations in the outer radiation belt, *J. Geophys. Res.*, *103*, 26,261–26,270, doi:10.1029/97JA02873.
- Ridley, A. J., and M. W. Liemohn (2002), A model-derived storm time asymmetric ring current driven electric field description, *J. Geophys. Res.*, *107*(A8), 1151, doi:10.1029/2001JA000051.
- Ridley, A. J., T. Gombosi, and D. Dezeew (2004), Ionospheric control of the magnetosphere: Conductance, *Ann. Geophys.*, *22*, 567–584.
- Roederer, J. G. (1970), *Dynamics of Geomagnetically Trapped Radiation*, Springer, Berlin.
- Rowland, D. E., and J. R. Wygant (1998), Dependence of the large-scale, inner magnetospheric electric field on geomagnetic activity, *J. Geophys. Res.*, *103*, 14,959–14,964, doi:10.1029/97JA03524.
- Stern, D. P. (1975), The motion of a proton in the equatorial magnetosphere, *J. Geophys. Res.*, *80*, 595–599.
- Toffoletto, F., S. Sazykin, R. Spiro, and R. Wolf (2003), Inner magnetospheric modeling with the Rice Convection Model, *Space Sci. Rev.*, *107*, 175–196, doi:10.1023/A:1025532008047.
- Tóth, G., et al. (2005), Space Weather Modeling Framework: A new tool for the space science community, *J. Geophys. Res.*, *110*, A12226, doi:10.1029/2005JA011126.
- Tóth, G., D. L. De Zeeuw, T. I. Gombosi, and K. G. Powell (2006), A parallel explicit/implicit time stepping scheme on block-adaptive grids, *J. Comput. Phys.*, *217*, 722–758, doi:10.1016/j.jcp.2006.01.029.
- Tóth, G., et al. (2012), Adaptive numerical algorithms in space weather modeling, *J. Comput. Phys.*, *231*, 870–903, doi:10.1016/j.jcp.2011.02.006.
- Tsyganenko, N. A. (1995), Modeling the Earth's magnetospheric magnetic field confined within a realistic magnetopause, *J. Geophys. Res.*, *100*, 5599–5612, doi:10.1029/94JA03193.
- Tsyganenko, N. A. (2002), A model of the near magnetosphere with a dawn-dusk asymmetry: 1. Mathematical structure, *J. Geophys. Res.*, *107*(A8), 1179, doi:10.1029/2001JA000219.
- Tsyganenko, N. A., and D. P. Stern (1996), Modeling the global magnetic field of the large-scale Birkeland current systems, *J. Geophys. Res.*, *101*, 27,187–27,198, doi:10.1029/96JA02735.
- Tsyganenko, N. A., H. J. Singer, and J. C. Kasper (2003), Storm-time distortion of the inner magnetosphere: How severe can it get?, *J. Geophys. Res.*, *108*(A5), 1209, doi:10.1029/2002JA009808.
- Vapirev, A. E., and V. K. Jordanova (2007), Calculation of bounce-averaged velocities and hydrogen densities for a storm-time magnetic field, *Geophys. Res. Lett.*, *34*, L10103, doi:10.1029/2007GL029380.
- Volland, H. (1973), A semiempirical model of large-scale magnetospheric electric fields, *J. Geophys. Res.*, *78*, 171–180.
- Wygant, J., D. Rowland, H. J. Singer, M. Temerin, F. Mozer, and M. K. Hudson (1998), Experimental evidence on the role of the large spatial scale electric field in creating the ring current, *J. Geophys. Res.*, *103*, 29,527–29,544, doi:10.1029/98JA01436.
- Young, D. T., H. Balsiger, and J. Geiss (1982), Correlations of magnetospheric ion composition with geomagnetic and solar activity, *J. Geophys. Res.*, *87*, 9077–9096, doi:10.1029/JA087iA11p09077.
- Zaharia, S., V. K. Jordanova, M. F. Thomsen, and G. D. Reeves (2006), Self-consistent modeling of magnetic fields and plasmas in the inner magnetosphere: Application to a geomagnetic storm, *J. Geophys. Res.*, *111*, A11S14, doi:10.1029/2006JA011619.
- Zaharia, S., V. K. Jordanova, M. F. Thomsen, and G. D. Reeves (2008), Self-consistent geomagnetic storm simulation: The role of the induced electric fields, *J. Atmos. Sol. Terr. Phys.*, *70*, 511–518.
- Zhang, J., et al. (2007), Solar and interplanetary sources of major geomagnetic storms ($Dst \leq -100$ nT) during 1996–2005, *J. Geophys. Res.*, *112*, A10102, doi:10.1029/2007JA012321.

R. Ilie and R. M. Skoug, Space Science and Applications, Los Alamos National Laboratory, MS D466, PO Box 1663, Los Alamos, NM 87545, USA. (rilie@lanl.gov)

M. W. Liemohn and G. Toth, Department of Atmospheric, Oceanic, and Space Sciences, University of Michigan, 2455 Hayward St., Ann Arbor, MI 48109-2143, USA.